Rashba-like physics in condensed matter

Gustav Bihlmayer[1], *Paul Noël*[2], *Denis V. Vyalikh*[3,4], *Evgueni V. Chulkov*[3,5] *and Aurélien Manchon*[6]✉

Abstract | Spin–orbit coupling induces a unique form of Zeeman interaction in momentum space in materials that lack inversion symmetry: the electron's spin is locked on an effective magnetic field that is odd in momentum. The resulting interconnection between the electron's momentum and its spin leads to various effects such as electric dipole spin resonance, anisotropic spin relaxation and the Aharonov–Casher effect, but also to electrically driven and optically driven spin galvanic effects. Over the past 15 years, the emergence of topological materials has widened this research field by introducing complex forms of spin textures and orbital hybridization. The vast field of Rashba-like physics is now blooming, with great attention paid to non-equilibrium mechanisms such as spin-to-charge conversion, but also to nonlinear transport effects. This Review aims to offer an overview of recent progress in the development of condensed matter research that exploits the unique properties of spin–orbit coupling in non-centrosymmetric heterostructures.

[1]*Peter Grünberg Institut and Institute for Advanced Simulation, Forschungszentrum Jülich and JARA, Jülich, Germany.*

[2]*Department of Materials, ETH Zurich, Zurich, Switzerland.*

[3]*Donostia International Physics Center (DIPC), Donostia–San Sebastián, Spain.*

[4]*IKERBASQUE, Basque Foundation for Science, Bilbao, Spain.*

[5]*Departamento de Polímeros y Materiales Avanzados: Física, Química y Tecnología, Facultad de Ciencias Químicas, Universidad del País Vasco UPV/EHU, Donostia–San Sebastián, Spain.*

[6]*Aix-Marseille Université, CNRS, CINaM, Marseille, France.*

✉*e-mail: aurelien.manchon@univ-amu.fr*

https://doi.org/10.1038/s42254-022-00490-y

Spin–orbit coupling is a relativistic effect that connects the spin angular momentum of the charge carrier with the electrostatic potential of its environment. Thus, it can be and has been used for spin manipulation, mainly guided by the ideas put forward by Emmanuel Rashba and co-workers. Intensive efforts have been pursued over the past decade to design and harvest spin–orbit coupling in condensed matter systems. In materials lacking a centre of inversion, this interaction adopts a unique form loosely called Rashba-like spin–orbit coupling that opens a particularly rich playground for scientists and materials engineers by unlocking new functionalities[1,2]. In the past few years, the field of 'Rashba physics' has progressively widened, in terms of mechanisms, materials and effects that can be exploited for potential applications. As the basic principles of Rashba physics have been addressed in detail in recent literature, we focus this Review on the most recent advances in the three areas mentioned above. We encourage readers unfamiliar with standard Rashba physics to refer to the numerous reviews already available on these aspects[1–3], as well as to the Supplementary Information, which also includes a short historical overview of the field.

We begin this Review by addressing new ideas that focus on the origin of Rashba spin–orbit coupling, deriving concepts to control and optimize it. Conventionally, the term 'Rashba effect' refers to a spin splitting that is linear in momentum, but when atomic orbitals of general symmetry (such as *p* or *d*) are involved, higher-order effects are observed. Besides these effects, newly discovered materials are then discussed, including 2D 'Janus' monolayers, centrosymmetric crystals with inversion partners in their unit cell, materials exhibiting orbital angular momentum texture, and materials that display Rashba-like spin textures even in the absence of spin–orbit coupling.

The development of these new concepts is in part driven by the widening of the basis of materials that have been recently synthesized, such as topological materials, which share the large spin–orbit coupling and the spin–momentum locking scheme with traditional Rashba systems. An interesting twist is obtained in magnetic materials, where the magnetization direction is a new degree of freedom to manipulate the spin textures in conventional and topological materials. We also cover strongly correlated materials, including *f* systems and superconductors, which have come increasingly into the focus of research over the past decade.

Although the discussion up to this point has been focused on states in equilibrium, non-equilibrium effects are central to the operation of new spin-based devices. The final section is devoted to these phenomena and starts with the interconversion of spin and charge currents by the Rashba effect, based on the materials discussed in the previous section. Besides responses to (static) electric fields, optical excitations in materials with large Rashba effect offer a wide field of applications, such as in hybrid perovskite solar cells. Optical techniques, such as gating and Floquet engineering, can also be used to to manipulate the magnitude of the Rashba spin–orbit coupling.

Key points

- The Rashba effect is a mechanism that locks the spin of a charge carrier to its momentum and stems from the coexistence of inversion symmetry breaking and spin–orbit coupling.
- The Rashba effect is ubiquitous in condensed matter and exists in a wide variety of systems and heterostructures, including semiconductors, metals, superconductors and correlated materials.
- The physics of the Rashba effect is at the origin of several important phenomena in condensed matter, including spin-to-charge interconversion, non-reciprocal magnetoelectric and magnetoptical response, and anomalous nonlinear effects.
- Depending on the crystal and magnetic symmetries of the system under consideration, complex forms of spin–momentum locking and dispersion can be obtained, leading to a rich zoo of phenomena.
- The impact of the Rashba effect extends far beyond spin transport and is at the basis of several key concepts in topological insulators, semimetals and superconductors.

Floquet engineering
Modification of the electronic band structure on shining off-resonant light on a material.

Bloch states
Solutions of the Schrödinger equation in the presence of a periodic potential, which characterize electrons in crystals.

Although this Review cannot address all active areas in the field of Rashba physics, nor foresee all possibilities for future developments, we conclude with an outlook on developments that could dominate this branch of research in the near future.

Microscopic origin

Principles

The central feature of Rashba-like spin–orbit interaction is the linear coupling between the carrier's spin angular momentum $\boldsymbol{\sigma}$ and its linear momentum $\mathbf{k}$ (REFS.[1,2]). In other words, the electron's spin and linear momenta are 'locked' on each other (BOX 1). The traditional form of Rashba spin–orbit coupling at interfaces (including surfaces) reads

$$H_{\mathrm{R}} = \alpha_{\mathrm{R}} \boldsymbol{\sigma} \cdot (\mathbf{k} \times \mathbf{z}), \tag{1}$$

where $\mathbf{z}$ is normal to the interface and the Rashba constant α_{R} contains all material-dependent parameters (in this case the surface potential gradient). A popular picture states that for an electron moving near an interface, the electric field $\mathbf{E}_{\mathrm{int}}$ associated with the interfacial potential gradient is transformed to a magnetic field $-\hbar/mc^2(\mathbf{k} \times \mathbf{E}_{\mathrm{int}})$ that couples to the electron spin, $\boldsymbol{\sigma}$. The Bychkov–Rashba (BR) model given in equation (1) qualitatively captures the effects seen experimentally on surfaces such as Au(111), where an almost free-electron-like surface state can be observed with angle-resolved photoemission spectroscopy (ARPES) and both the predicted spin splitting and the spin texture can be confirmed[4,5]. However, quantitatively the estimates of α_{R} from the BR model are orders of magnitude too small. The observation[6] that α_{R} is 10 times larger for Au(111) than for Ag(111) — although the work functions are similar — indicates that something is missing in this picture.

The fact that relativistic effects are larger in heavy atoms (such as Au) than in lighter ones (such as Ag) results from the steeper potential gradients at the nucleus when the atomic number Z is large. In an atom, the spin–orbit coupling interaction reads $H_{\mathrm{so}} \approx \xi \boldsymbol{\sigma} \cdot \mathbf{L}$, where $\mathbf{L}$ and $\boldsymbol{\sigma}$ are the orbital and spin angular momenta, respectively, and ξ is the spin–orbit coupling parameter that scales approximately as $Z^{2.4}$ (REF.[7]). In this limit, which is widely valid in all materials of interest, the Rashba spin–momentum locking appears as a consequence of the momentum-dependent orbital angular momentum induced by the inversion symmetry breaking. In fact, in the basis of the Bloch states $|\psi_{n,\mathbf{k}}\rangle$, the spin–orbit coupling can be rewritten

$$\langle \psi_{n,\mathbf{k}} | H_{\mathrm{so}} | \psi_{n,\mathbf{k}} \rangle = \xi \boldsymbol{\sigma} \cdot \mathbf{L}_n(\mathbf{k}) = \mu_{\mathrm{B}} \boldsymbol{\sigma} \cdot \mathbf{B}^n_{\mathrm{so}}(\mathbf{k}), \tag{2}$$

where $\mathbf{L}_n(\mathbf{k})$ and $\mathbf{B}^n_{\mathrm{so}}(\mathbf{k})$ are the band- and momentum-dependent orbital momentum and effective magnetic field, respectively. In other words, the spin–orbit coupling mimics the effect of a Zeeman term with a momentum-dependent magnetic field that is merely proportional to a (momentum-dependent) orbital moment, $\mathbf{B}^n_{\mathrm{so}}(\mathbf{k}) = (\xi/\mu_{\mathrm{B}})\mathbf{L}_n(\mathbf{k})$. The emergence of this momentum-dependent orbital moment can be understood straightforwardly on considering that close to the nucleus, where spin–orbit coupling is effective, Bloch states are well described by a linear combination of atomic orbitals. A non-vanishing orbital momentum is obtained through the intra-atomic hybridization of two orbitals with orbital number l and different magnetic numbers m (such as $L_k = \mathrm{i}\varepsilon_{ijk}\langle p_i|\mathbf{L}|p_j\rangle$ and so on). This hybridization needs to be mediated by an intermediate orbital, and various scenarios are possible (FIG. 1 and BOX 1).

The effective field in Rashba spin–orbit coupling is characterized by its antisymmetry with respect to $\mathbf{k}$: $\mathbf{B}^n_{\mathrm{so}}(\mathbf{k}) = -\mathbf{B}^n_{\mathrm{so}}(-\mathbf{k})$, a property that only emerges under inversion symmetry breaking. As an illustration, consider an interface between dissimilar materials, normal to z. This interface has mirror symmetries along x and y and a continuous rotation about z. As the magnetic field is an axial vector (and we consider only in-plane momenta), it must lie in the (x,y) plane

Box 1 | **Microscopic picture of Rashba spin–orbit coupling**

A traditional representation of the microscopic origin of Rashba spin–orbit coupling states that the potential gradient at an interface is dominated by the electric field normal to this interface, $\mathbf{E}_{\mathrm{int}} = -\partial_z V \mathbf{z}$, resulting in the transformation of the spin–orbit coupling

$$H_{\mathrm{so}} = \frac{e\hbar}{(2mc)^2} \boldsymbol{\sigma} \cdot (\nabla \mathbf{V}(\mathbf{r}) \times \mathbf{p}) \rightarrow H_{\mathrm{so}} = \partial_z V \frac{e\hbar}{(2mc)^2} \boldsymbol{\sigma} \cdot (\mathbf{z} \times \mathbf{p}) \tag{5}$$

with e the charge on the electron and m its mass. This argument is incorrect as the potential gradient in solid state is always dominated by the potential drop close to the nucleus and in fact retains a spherical symmetry, $\nabla \mathbf{V}(\mathbf{r}) \approx (1/r)\partial_r V \mathbf{r}$, even close to an interface. Therefore, the spin–orbit coupling term is most likely to adopt the usual Russell–Saunders scheme, $H_{\mathrm{SO}} = \xi \boldsymbol{\sigma} \cdot \mathbf{L}$. In other words, the interfacial potential gradient does not affect the spin–orbit coupling itself, but rather the Bloch wavefunction of the conduction electrons such that they acquire a momentum-dependent orbital moment, $\mathbf{L}_n(\mathbf{k})$, as explained in the main text.

FIGURE 1 illustrates two representative scenarios for the generation of Rashba spin–orbit coupling. It is sufficient to design a mechanism that enables a $\mathbf{k}$-antisymmetric orbital momentum, $\mathbf{L}_n(\mathbf{k}) = -\mathbf{L}_n(-\mathbf{k})$. The simplest way to obtain an atomic orbital moment is to mix orthogonal orbitals. For example, mixing p_x and p_z orbitals would result in non-vanishing L_y. In addition, to ensure that this mixture is antisymmetric in momentum space, one needs to break the inversion symmetry either by applying an external electric field (electrostatic inversion symmetry breaking) or through asymmetric hybridization (geometrical inversion symmetry breaking). Whereas the first scenario qualitatively applies to the surface of Ag and Au (REF.[9]), in real materials both scenarios are likely to be present to various degrees, involving d orbitals and complex charge-transfer schemes. The spin–momentum locking scheme therefore depends on the chemical bonding and electrostatic environment, resulting in diverse spin textures in momentum space.

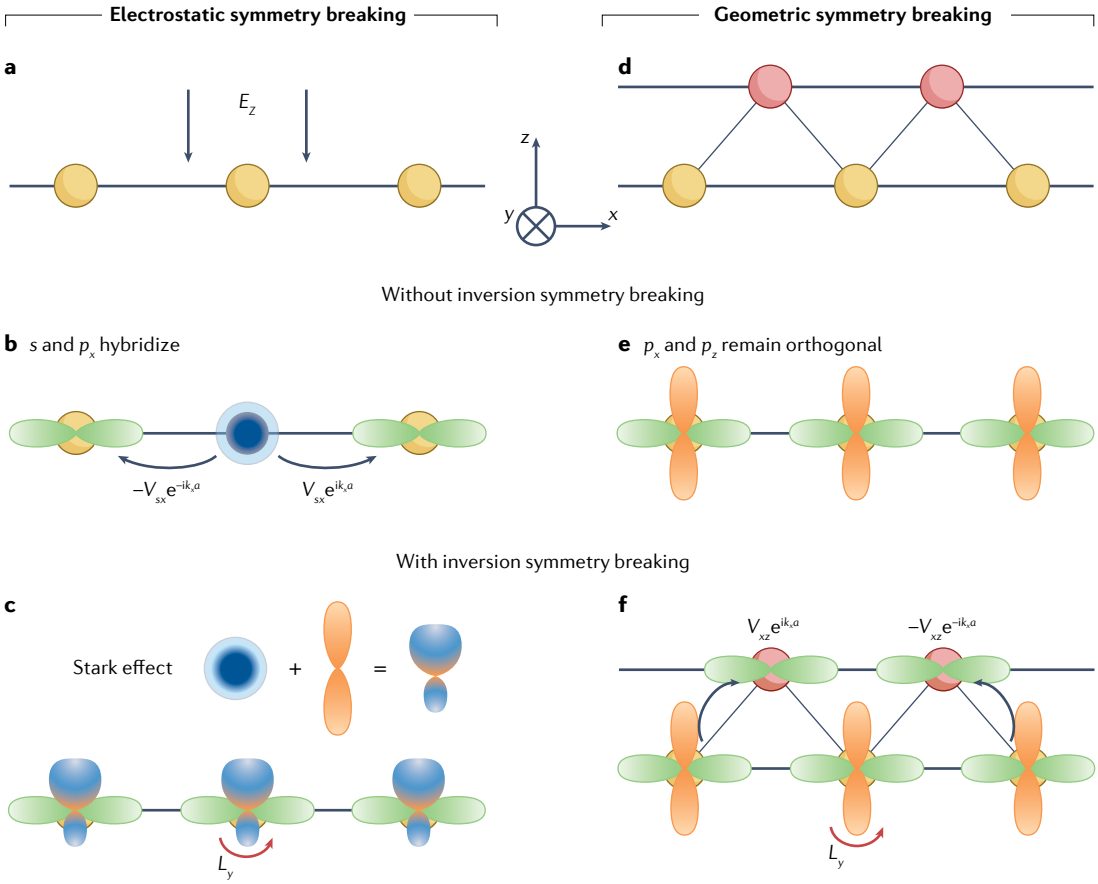

Fig. 1 | **Electrostatic and geometric symmetry breaking giving rise to k-antisymmetric orbital momentum and Rashba-like spin–orbit coupling. a** | A monoatomic chain possessing s, p_x and p_z orbitals. **b** | By construction, the interatomic overlap between the s and p_x orbitals is antisymmetric in momentum **k**, $\langle s|H|p_x\rangle = -2iV_{sx}\sin k_x a$. **c** | Applying an external field breaks the inversion symmetry, which turns on intra-atomic s–p_z orbital mixing via the Stark effect. As a result, p_x and p_z hybridize, mediated by the s orbitals, giving rise to a **k**-antisymmetric orbital momentum L_y. In the presence of spin–orbit coupling, this orbital momentum couples to the spin momentum, yielding Rashba-like spin–momentum locking. **d** | Two coupled atomic chains possessing both p_x and p_z orbitals. **e** | In an individual chain, the p_x and p_z orbitals remain orthogonal to each other and are uncoupled, resulting in zero orbital momentum. **f** | When coupling the two chains, inversion symmetry breaking is naturally introduced so that the interatomic overlap between, say, the top p_x and bottom p_z orbitals is antisymmetric in momentum **k**, $\langle p_z|H|p_x\rangle = -2iV_{xz}\sin k_x a$, enabling a **k**-antisymmetric orbital momentum L_y on the bottom chain. Again, upon turning on spin–orbit coupling, Rashba-like spin–momentum locking emerges.

and therefore, to the first order in momentum, it reads $\mathbf{B}^n_{so}(\mathbf{k}) = (b_{xx}k_x + b_{xy}k_y)\mathbf{x} + (b_{yx}k_x + b_{yy}k_y)\mathbf{y}$. Applying the two in-plane mirror symmetries $\mathcal{M}_{x,y}$, one obtains

$$\mathcal{M}_x\mathbf{B}^n_{so}(\mathcal{M}_x\mathbf{k}) = (-b_{xx}k_x + b_{xy}k_y)\mathbf{x} - (-b_{yx}k_x + b_{yy}k_y)\mathbf{y}, \quad (3)$$

$$\mathcal{M}_y\mathbf{B}^n_{so}(\mathcal{M}_y\mathbf{k}) = -(b_{xx}k_x - b_{xy}k_y)\mathbf{x} + (b_{yx}k_x - b_{yy}k_y)\mathbf{y}. \quad (4)$$

Considering Neumann's principle, $\mathcal{M}_{x,y}\mathbf{B}^n_{so}(\mathcal{M}_{x,y}\mathbf{k}) = \mathbf{B}^n_{so}(\mathbf{k})$, and we get $b_{xx} = b_{yy} = 0$. In addition, if we impose continuous rotation about the z axis, we get $b_{xy} = -b_{yx} = b_0$ and $\mathbf{B}^n_{so}(\mathbf{k}) = b_0(k_y\mathbf{x} - k_x\mathbf{y}) = b_0(\mathbf{k}\times\mathbf{z})$, as expected at an interface. Naturally, adding more symmetries and expanding the effective magnetic field beyond the first order in momentum yields much richer expression and spin–momentum locking configurations.

Neumann's principle
The physical properties of a crystal should possess at least the same symmetries as the crystal itself.

The first microscopic scenario for Rashba spin splitting at the surface of Au was based on an (s,p) tight-binding model. This model states that α_R is indeed proportional to the product of the spin–orbit coupling strength, ξ, and a term that characterizes the inversion symmetry breaking[8]. The size of the latter can be shown to be determined by the asymmetry of the wavefunction under study at or near the position of the nucleus[9]. This is influenced by the external field and the orbital character of the wavefunction[10].

Up to now, free electrons or electrons of s- or p_z-like symmetry were considered that do not carry an orbital momentum without symmetry breaking. At the top of the valence band of a semiconductor like Ge, however, three p orbitals form a six-fold degenerate state that is split by spin–orbit coupling into a doubly degenerate one (total orbital momentum $m_j = 1/2$) and a four-fold degenerate ($m_j = 3/2$) one, like in a free atom. Because the top of the valence band is at $k = 0$, no additional orbital moment arises when inversion symmetry is broken.

Moving away from the zone centre to finite **k**, the superposition of the 'atomic' orbital momentum and the '*k*-induced' one leads to interesting effects[11]. In surface systems, this can be nicely studied in the $BiAg_2$/Ag(111) surface alloy, which shows one of the largest observed Rashba splittings in the *s* band[12]. The higher-lying *p* bands have a rich spin- and orbital texture that can also be observed experimentally[13]. The spin splitting in this case is not necessarily linear in *k* but can be cubic as well. Large Rashba-like spin splitting of the *p* bands has been also reported in bulk materials, such as BiTeI (REF.[14]) and GeTe (REF.[15]), the latter being electrically switchable[16].

The specific scenarios discussed above exemplify the physical origin of Rashba-like spin splitting in selected systems, but they fail to provide a more general, systematic theory. A crucial question that remains unsatisfactorily addressed concerns the means and strategies to control and maximize the magnitude of the Rashba-like parameter. From this model, it is clear that materials possessing heavy elements (Pt, Au, Bi, Pb) tend to display larger spin splitting due to their large atomic spin–orbit coupling, as confirmed in experiments, but this model says nothing about the role of the non-centrosymmetric electrostatic potential that surrounds these atoms.

In fact, optimizing the strength of Rashba spin–orbit coupling requires a fine understanding of the interplay between the atomic spin–orbit coupling, which locks the spin momentum on the orbital angular momentum direction, and the (non-centrosymmetric) crystal field, which lifts the degeneracy of the orbital angular momentum. FIGURE 2, inspired by REF.[17], aims to provide a qualitative picture of the competition between these two terms.

In most materials possessing large atomic spin–orbit coupling, the inversion-breaking crystal field acts as a perturbation so that the resulting Rashba-like spin splitting is only a fraction of the spin–orbit energy. In contrast, if one can achieve a large crystal field, the spin–orbit coupling acts as a perturbation, and therefore the spin splitting takes full advantage of the atomic spin–orbit interaction. Consequently, an optimal compromise between these two energy scales will maximize the Rashba-like spin splitting. It has been proposed that such a maximal Rashba spin splitting is obtained in $PtCoO_2$ (REF.[17]). Along a different line of thought, other work suggests that the hallmark of a large Rashba spin splitting in bulk materials is the existence of avoided band crossings in the electronic structure[18]. This interesting observation confirms that orbital mixing is a key ingredient to design materials with large Rashba-like spin–orbit coupling. Although a complete theory offering clear guidelines for the design of maximized Rashba spin splitting in bulk and at interfaces remains to be established, these two works point out inspiring directions that need to be further developed.

Beyond linear Rashba

As mentioned above, the effective Hamiltonian for the BR model contains terms of the form $(\sigma_x k_y - \sigma_y k_x)$. If symmetry is higher, such as $\bar{4}3m$, other terms like $k_x(k_y^2 - k_z^2)\sigma_x$ are obtained (Dresselhaus effect[19]). Note that the point-group symmetry is here determined by the subgroup of the *k* point around which the $\mathbf{k}\cdot\mathbf{p}$ model is developed. Each of these Hamiltonians defines a specific relation between spin- and crystal momentum (spin–momentum locking), and these relations can be used to tailor spin properties. For example, a combination of Rashba and Dresselhaus terms can be chosen that leads to a uniform spin direction for all **k** vectors minimizing spin relaxation[20]. This minimization of the spin relaxation can also be achieved with other, 'cubic Rashba' terms that appear for certain symmetry groups. A nice overview of the different terms that can appear depending on symmetry can be found in the supplemental material of REF.[21]. Similar to early work[22] that analysed different *k* points in the Brillouin zone, a rich variety

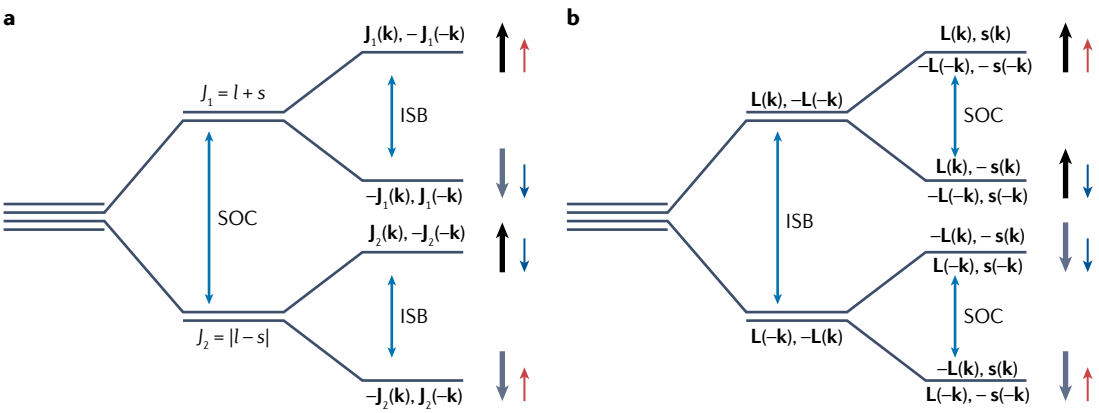

Fig. 2 | **Schematics of the interplay between inversion symmetry breaking and spin–orbit coupling.** The grey and black arrows represent the orbital angular momentum; red and blue arrows represent spin angular momentum. **a** | When the spin–orbit coupling dominates, it hybridizes the orbital and spin angular momenta and splits states with different total angular momentum *J*. Turning on the crystal field and breaking inversion symmetry further splits states with opposite momentum **k**. **b** | When the non-centrosymmetric crystal field dominates, it first lifts the degeneracy between orbital states with opposite momentum **k**. Turning on the spin–orbit coupling further then splits the states whose spin **s** is parallel and antiparallel with the orbital angular momentum **L**. This sketch is only meant to provide a qualitative picture of the respective roles of inversion symmetry breaking and spin–orbit coupling. Applying this analysis to a realistic system (involving, for example, *p* or *d* orbitals) results in much more complex energy diagrams. ISB, inversion symmetry breaking; SOC, spin–orbit coupling.

of dispersion laws can be found. Further away from high-symmetry points, one is not limited by symmetry constraints, and more exotic effects can be found, such as a triple winding of the spin texture that can also be described by a cubic Rashba model[23,24] (see also below).

Another aspect, which goes beyond the classical BR model, is the possibility of realizing 3D spin structures. When the electric field is not restricted to a single direction (such as perpendicular to the surface), the electron spin is no longer confined to a plane (in this case, the surface) even if we assume that the electron motion is strictly 2D. For example, molecular adsorption on a surface can tilt the spin from in- to out-of-plane when the molecules induce an in-plane oriented electric field[25]. In ferroelectric materials, the switchable polarization also offers the possibility of manipulating the spin texture of the bands[26]. One can expect that the prospect of using this variety of effects in spintronic applications will lead to more discoveries.

Janus configuration in 2D materials

The rise of 2D materials and van der Waals heterostructures has opened new avenues for the engineering of Rashba spin splitting at the atomic scale[27]. Transition metal dichalcogenides[28], trihalides[29] or phosphorus trichalcogenides[30], for instance, represent promising classes of material as they are composed of a hexagonal lattice of metallic elements embedded between two layers of chalcogens (S, Se, Te) or halides (Cl, Br, I). In pristine configuration, these monolayers do not display Rashba-type spin splitting as they are either centrosymmetric (1T) or non-centrosymmetric (2H), the planar mirror symmetry in the latter forbidding Rashba-type spin splitting. Nonetheless, it is possible to induce Rashba-type spin splitting by differentiating the chalcogen or halide elements on each side of the metallic plane[31]. This structure, called the Janus configuration, has been predicted and realized experimentally in non-magnetic transition metal dichalcogenides[32–34]. The dissimilarity between the electronegativity of the two chalcogen or halide elements induces an electric dipole perpendicular to the plane of the monolayer and promotes a reasonably large Rashba-type spin–orbit coupling.

Hidden spin polarization in centrosymmetric crystals

It is worth mentioning that inversion symmetry breaking does not necessarily apply globally but can also emerge locally. In this case, this local breaking of inversion symmetry can lead to local Rashba spin–orbit coupling, but no band-structure spin splitting. In other words, the absence of spin splitting does not preclude the existence of a local Rashba-like effect within the unit cell. As a matter of fact, as the Rashba effect is dictated by the local inversion symmetry breaking rather than by global inversion symmetry breaking, certain centrosymmetric crystals display so-called hidden spin polarization[35]. An illustrative example is that of Si, a crystal whose motif is composed of two sites that are inversion partners such that they individually experience inversion symmetry breaking of opposite polarity. In other words, each inequivalent Si ion experiences a Rashba-like spin–momentum locking of its own. To distinguish these hidden spin textures from the conventional Rashba and Dresselhaus textures obtained in non-centrosymmetric materials, the hidden spin–momentum locking is sometimes referred to as R-2 (for Rashba symmetry) and D-2 (for Dresselhaus symmetry)[35].

This observation can be extended to many more materials possessing atoms with non-centrosymmetric space group. Examples concern centrosymmetric non-magnetic materials such as NaCaBi and $LaOBiS_2$. A hidden spin polarization texture, pointing perpendicular to the stacking plane, has been reported in centrosymmetric WSe_2 at K and K′ points of the Brillouin zone[36]. More recently, a hidden in-plane spin texture mimicking the Rashba spin–momentum locking has been observed in the high-temperature superconductor bismuth strontium calcium copper oxide (B2212)[37]. This effect is particularly spectacular in Mn_2Au and CuMnAs antiferromagnets, where the Mn ions carrying the magnetic moment are inversion partners[38,39]. In these two crystals, the hidden polarization induced by spin–orbit coupling leads to a current-driven effective field of opposite sign on the two inversion partners. Because the Mn ions are magnetic, the staggered effective magnetic field induces a local torque that can trigger magnetization switching[39,40]. This research direction is currently gaining momentum due to its potential for ultrafast applications[41,42].

Orbital Rashba effect

The conceptual separation of spin–orbit coupling and inversion symmetry breaking is also used in studies focusing on the orbital Rashba effect[43,44]. Here, the formation of an orbital angular momentum $\mathbf{L}$ is seen as a first step and described by a model Hamiltonian $\alpha_K(\mathbf{k}\times\mathbf{L})\cdot\mathbf{E}$ where α_K quantifies the coupling to the electric field. At a given wavevector $\mathbf{k}$, Kramers pairs of states obtain a preferred orbital momentum $\mathbf{L}$ (and $-\mathbf{L}$ at $-\mathbf{k}$), and the spin–orbit coupling term splits these pairs further, minimizing or maximizing $\boldsymbol{\sigma}\cdot\mathbf{L}$ (FIG. 2)[43]. Again, one can obtain some insight into the origin of the orbital Rashba constant, $\alpha_{OR}=\alpha_K E$, by studying a 2D (s,p) tight-binding model[45]. Like in the model of REF.[8], it is proportional to hopping matrix elements that vanish in the limit of an inversion-symmetric system (such as the hopping from s to p_z when the model is downfolded on p_z orbitals).

In the band structure, the orbital Rashba effect manifests itself by an antisymmetric orbital texture in the Brillouin zone, similar to the spin texture characterizing the Rashba spin–orbit interaction. This texture is illustrated in FIG. 3 for a model of Ag_2Bi introduced elsewhere[45]. The spin-splitting bands display spin textures of opposite chirality (FIG. 3c,e), whereas the chirality of the orbital texture remains unchanged (FIG. 3b,d). This orbital texture in momentum space enables the generation of non-equilibrium orbital polarization even in the absence of spin–orbit coupling. Together with its parent effect, the orbital Hall effect[43,46], the orbital Rashba effect[47,48] is now gaining increasing attention as it could be used to induce interconversion between charge currents and orbital currents.

Orbital Hall effect
Generation of a pure orbital current transverse to an injected charge current.

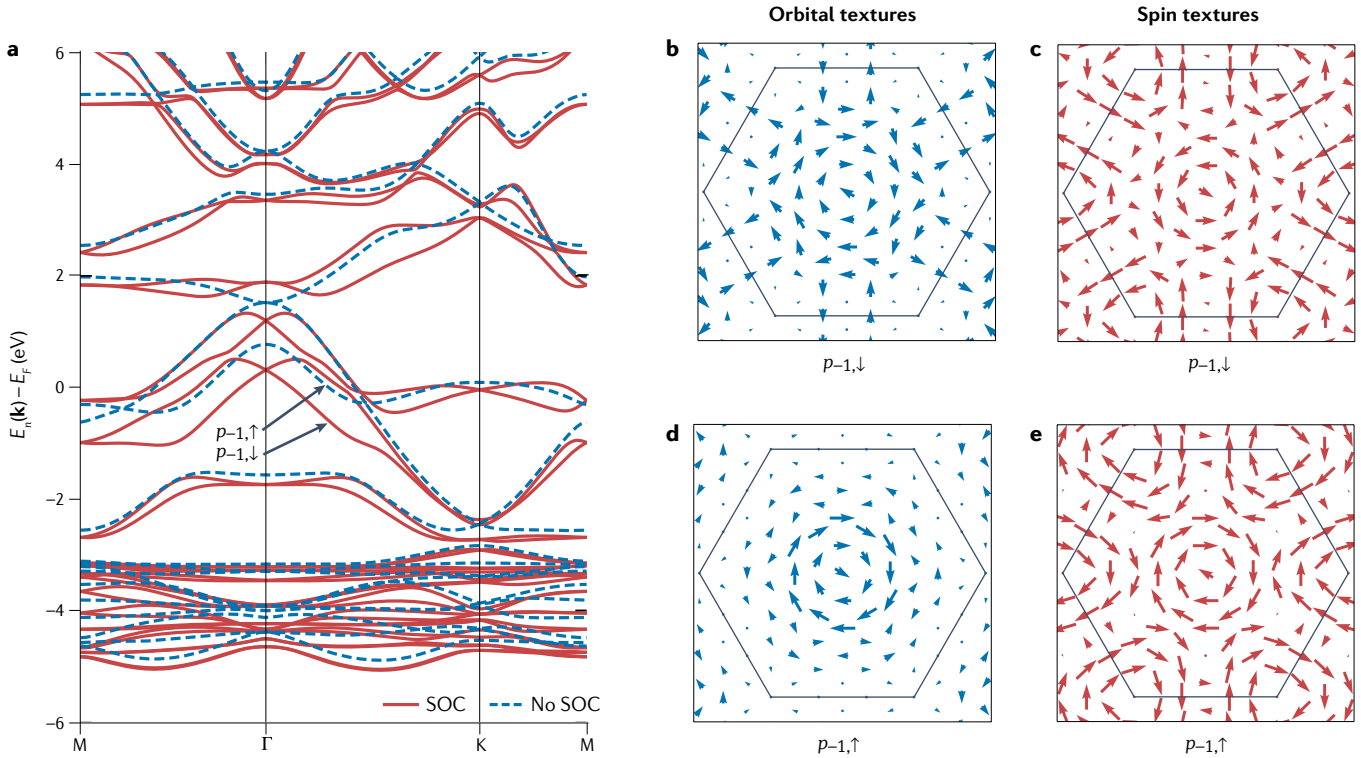

Fig. 3 | **Spin and orbital textures in momentum space. a** | Band structure obtained from an (*s*,*p*) tight-binding model for Ag_2Bi, with (red) and without (dashed blue) spin–orbit coupling. **b**–**e** | Orbital (**b**,**d**) and spin (**c**,**e**) textures in momentum space for two selected bands, $p_{-1,\uparrow}$ and $p_{-1,\downarrow}$, as indicated in panel **a**. Adapted with permission from REF.[45], under a Creative Commons licence CC BY 4.0.

Rashba effect without spin–orbit coupling

In fact, spin–orbit coupling is not even necessary to obtain an antisymmetric spin texture in momentum space. The key ingredient is to break the U(1) spin rotational symmetry to ensure that the spin angular momentum is not a good quantum number. Besides spin–orbit coupling, magnetism can also break the spin rotational invariance, resulting in a spin texture in momentum space[49–51]. This exchange-induced momentum-dependent spin splitting has been reported[52,53] in several collinear antiferromagnets such as RuO_2. In this class of compounds, the electron spin is aligned along the Néel order, and it is therefore different from the Rashba-like spin splitting discussed in this Review (see discussion elsewhere[54]).

To obtain a momentum-dependent spin texture, that is, a variation of the spin direction over the Brillouin zone, one rather needs to consider (antiferro)magnets presenting a non-collinear magnetic structure, such as Mn_3Sn or Mn_3Ir (REF.[55]). The resulting spin texture possesses the same symmetries as the magnetic configuration and remains inversion-symmetric. On breaking the spatial inversion symmetry, antisymmetric spin–momentum locking appears in antiferromagnets[56].

New materials for Rashba physics

Connection between Rashba and Dirac physics in topological materials

Wide classes of materials display the signature of Rashba-like physics in their band structure and electronic transport properties. Materials with non-trivial ground-state topology[57,58] usually host interfacial states that behave very similarly to Rashba states. Before addressing these materials, let us briefly summarize some of the most important manifestations of the Rashba effect. First, an energy splitting is observed for states with a finite crystal momentum. At the zone centre ($k = 0$) or halfway between two zone centres, this energy splitting is zero. Second, there is a fixed relation between momentum and spin (spin–momentum locking) of the moving electron, even in the non-magnetic case. These two effects are a consequence of spin–orbit coupling and manifest in particular at the surface of a crystal, where some symmetries are broken.

These manifestations can be used to realize special transport properties at the boundary of a sample. For instance, when a small magnetic field perpendicular to the spin directions lifts the degeneracy of the two states at $k = 0$ (BOX 2, panel d) and the Fermi level is placed in this gap, only two states are left at this energy, possessing opposite spin. This leads to a persistent spin current at the edge of the sample, in remarkable analogy to what is observed in 2D topological insulators (see below). Indeed, this concept was proposed as a way to realize topological superconductivity by bringing semiconductor nanowires with strong spin–orbit coupling (like InSb) into contact with conventional *s*-wave superconductors and applying an external magnetic field[59,60]. This setting was realized experimentally[61] and, since then, has been used as a platform for hunting Majorana fermions in various setups[62]. Very similar proposals

Photogalvanic effect
Generation of a DC charge current on shining linearly or circularly polarized light on a material.

Quantum spin Hall effect
Transport mechanism associated with insulating bulk states and topologically protected spin-current carrying edges or surface states.

Quantum anomalous Hall effect
Transport mechanism associated with insulating bulk states and topologically protected charge-carrying edges or surface states.

use topological insulators in contact with conventional superconductors, without the need to apply a magnetic field[63] or to find natural topological superconductors[64].

Because they both display strong antisymmetric spin–momentum locking, non-magnetic topological materials and Rashba systems share a lot of similarities, such as the response to magnetic fields of different orientation, direct and inverse Edelstein effects, spin-to-charge interconversion, the photogalvanic effect, or the possibility of showing higher-order (in k) effects. In addition, the quantum spin Hall effect (SHE) can be realized in Rashba systems like in the above-mentioned example or — a more complex example — the quantum anomalous Hall effect (AHE) in graphene coupled to external magnetic textures[65–67]. Both the quantum SHE and quantum AHE target the precise control of the (transported) electron's spin, which can be useful for spintronic applications. As compared with Rashba systems, however, topological materials benefit from topological protection of the electronic states.

In addition to topological insulators, topological semimetals have also been identified, in particular Dirac semimetals (DSM) and Weyl semimetals (WSM)[57]. In contrast to topological insulators, in semimetals the bulk spectrum already shows Dirac-cone-like energy nodes with a spin–momentum locking — for WSM of the form $H_{3D} \propto \mathbf{k} \cdot \boldsymbol{\sigma}$, meaning that the spin is (anti)parallel to the momentum — that offers new possibilities for spintronic applications[68]. In particular in WSMs, where the nodal points come in pairs, lack of time and inversion symmetry gives rise to exotic surface states and exciting transport properties.

Complex spin textures at the surface of topological materials

Non-magnetic topological insulators are 3D or/and 2D time-reversal-symmetric crystalline systems whose electronic structure is characterized by non-zero Z_2 topological invariant[69,70]. In these materials, spin–orbit interaction is strong enough to invert the fundamental energy gap and transform topologically trivial semiconductors into topological insulators. On the surface (edge) of a 3D (2D) topological insulator, this transformation induces a Dirac-cone state with spin–momentum locking that is the cornerstone for realization of the quantum SHE[69,70]. In fact, because time-reversal symmetry is preserved, the topological states at opposite surfaces (edges) are necessarily of opposite spin chirality and charge neutral. As a result, at a given surface (edge), states of opposite momentum carry an opposite spin, resulting in a Dirac cone with spin–momentum locking similar to the Rashba one. Typical representatives of 3D topological insulators are tetradymites such as Bi_2Te_3, Bi_2Se_3 and Sb_2Te_3, which are layered materials linked by van der Waals forces[71,72].

The essential surface/interface physics of topological insulators can be described by using a Rashba-like Hamiltonian (equation (1)) where the coefficient α_R

Box 2 | Combined effects of Rashba and Zeeman (or exchange) fields

More exotic effects can be observed when an exchange-split band (such as a bulk or quantum-well state) crosses the Rashba-split bands. Because of the spin-selective hybridization between these bands, asymmetric bandgaps open, leading to characteristic transport effects such as a strong anisotropic magnetoresistance and current-induced spin polarization[237]. In constant energy contours, this can result in the appearance of arc-like features that should not be mistaken for signatures of Weyl semimetals.

Depending on the respective energy scales of the Rashba effect and the exchange splitting, the former can influence the magnetic order of the atoms that give rise to the latter: Rashba spin–orbit coupling can give rise to a 'twisted exchange interaction'[238], which appears as a Dzyaloshinskii–Moriya interaction, meaning that it can lead to spin spirals if the anisotropy barriers can be overcome[239]. This is, of course, not surprising, as both the Rashba effect and the Dzyaloshinskii–Moriya interaction rely on a combination of inversion symmetry breaking and spin–orbit coupling.

The dispersion relations of a free-electron gas with Rashba and Zeeman fields[240] are illustrated here. Panel **a** shows the dispersion of the two branches of the Rashba- and Zeeman-split free-electron gas in the k_x direction, with red and blue indicating the spin orientation in the $+y$ and $-y$ directions, respectively. Panel **b** gives iso-energy cuts at an energy of 0.3 eV with the upper (lower) part showing the normalized S_x (S_y) components as line thickness (different orientations in red and blue). Panel **c** shows the location of the cuts in panels **a** and **b** in a 3D representation of $E(k_x,k_y)$. Panel **d** shows the dispersion along k_x with the upper (lower) panel indicating the normalized spin components in the y (z) direction. Panel **e** shows $E(k_x,k_y)$ with the cuts from **d** and two iso-energy contours that have circular shape. For all plots, $\alpha_R = 1.44$ eV Å, and the exchange is $JS = 0.5$ eV (**a**–**c**) and 0.1 eV (**d**,**e**).

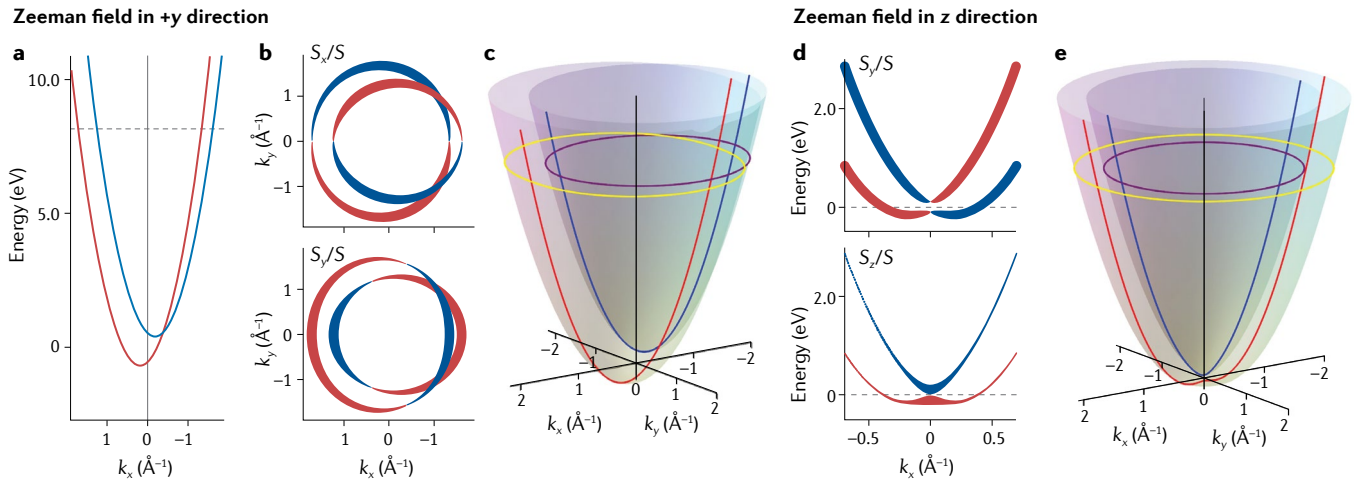

is substituted by the electron velocity v of the Dirac cone[73,74]. Consequently, spin–momentum locking in the Dirac-cone surface states is similar to that in the Rashba surface states and hence many physical properties of these two classes of surface states are similar. Some time-reversal-symmetry protected topological insulators demonstrate even more complicated behaviour of the topological surface state. In particular, photoemission measurements have shown strong hexagonal warping of the Dirac cone in Bi_2Te_3 that was also confirmed by ab initio calculations and model Hamiltonian simulations with terms at the third order in wavevector **k** (REFS.[73,74]). The warping results in the appearance of an out-of-plane spin moment component of the Dirac electron[73–75] which changes from up to down following the rotational symmetry of the crystal and does not produce a mass gap at the Dirac point.

The Weyl and Dirac semimetals can be viewed as extensions of the Rashba case, as spin–momentum locking remains a central ingredient that governs most of their remarkable properties. Topological semimetals are characterized by the Dirac-like spectra arising in the bulk and by the topological stability of the Fermi surface, if it encloses band crossing points, which are the Dirac-cone-like energy nodes. These systems can be identified by the momentum-space location of the nodal points and by degeneracy. The WSMs hold nodal points (magnetic monopoles) in pairs with opposite momenta **k** and opposite topological charge, while in the DSMs both opposite charges fall to one **k**, and thus the Dirac cone appears to be doubly degenerate. The Weyl nodes of opposite charge, separated in momentum space, are connected through the crystal boundary/surface by Fermi arcs, enabling direct and inverse Edelstein effects[76]. Since theoretical predictions of topological semimetals, many topological semimetallic systems have been experimentally investigated (see, for instance, representative reviews[57,58]).

Magnetic topological materials

Introduction of magnetic order into topological insulators breaks time-reversal symmetry and enables modifications of surface (interface) electronic structure that pave the way for new quantum effects such as quantum AHE[77,78], the topological magnetoelectric effect[77] and such phenomena as image magnetic monopole and axion electrodynamics[77]. These effects occur in topological insulators in which a time-reversal-symmetry breaking is realized with an out-of-plane magnetization component M_z. The respective electronic structure of the 3D topological insulator surface or thin-film topological insulator edge can be obtained from the Rashba Hamiltonian by adding a mass term $-m\sigma_z$, where m reflects the out-of-plane magnetization value, $m = JM_z$, where J is an interlayer exchange parameter[79]. The mass term results in gap formation at the Dirac-cone point and also the emergence of the gapless 1D mode at the topological insulator film edge within the formed energy gap (a pictoral representation is given in the Supplementary Information). The peculiar property of this mode is its chirality, which means that the electron can propagate along the edge only in one direction without backscattering. With the Fermi level fixed within the gap of the topological insulator surface state, this makes the effect advantageous for dissipationless transport applications, thus allowing realization of a quantized Hall conductivity. Another interesting configuration consists in considering a domain wall formed by two in-plane magnetic domains at the topological insulator surface. In this case, a vertically spin-polarized 1D flat electron state, characterized by the Dirac-cone velocity and the surface magnetization, arises at the domain wall[80,81]. When the Fermi level is pinned to the flat-band energy, one can expect the emergence of superconductivity driven by the coupling of heavy electrons from neighbouring domain walls.

There are various ways to introduce magnetic order into topological insulators, such as doping with magnetic atoms at the surface[79,82], in the near-surface region[75,83] or in the bulk[84,85]. Experimentally, however, quantum AHE and axion insulator states have been realized in this way only at temperatures below 2 K (REFS.[86–89]). More recently, a method based on the creation of 2D highly ordered ferromagnets as basic blocks for incorporation of magnetism into the topological insulator bulk or surface was proposed[90–92]. By placing the 2D ferromagnetic block on the tetradymite topological insulator surface, an efficient time-reversal symmetry breaking can be realized[90,91,93], producing a giant magnetic gap (up to 110 meV) in the Dirac cone due to a strong exchange interaction of this state with 3*d* moments. This approach, called magnetic extension[90], offers various advantages such as highly ordered crystal structure, absence of trivial surface or interface states, not affecting the topological insulator bulk-like region, and finally, a lot of possible heterostructures composed of magnetic and non-magnetic insulators. Moreover, in certain situations, these 2D ordered ferromagnets can be completed by magnetic atom doping to enhance the magnetization effect on the magnetic energy gap and Curie (Néel) temperature of the heterostructure. One of the recent and promising 2D magnetic systems, $Mn_4Bi_2Te_7$ grown on Bi_2Te_3, demonstrates Curie temperature of 20 K and a Dirac-cone gap of 40–75 meV (REF.[94]).

Another promising way for the realization of new quantum phenomena is the creation of topological insulators composed of 2D ferromagnetic multiple-atomic-layer blocks antiferromagnetically ordered in the direction perpendicular to the layers. The recent discovery of an intrinsic antiferromagnetic topological insulator, $MnBi_2Te_4$, with Néel temperature of 25 K and Dirac-cone gap of 80–90 meV (REF.[95]) has been a breakthrough in the field of magnetic topological insulators with great potential for realization of various quantum effects. Just after this discovery, new magnetic topological insulators, $(MnBi_2Te_4)(Bi_2Te_3)_m$, with $m = 1,\ldots,6$ (REF.[96]), and $MnSb_2Te_4$, $MnSb_4Te_7$ (REFS.[97,98]) were predicted and synthesized.

New physics and new effects can appear if an antiferromagnetic topological insulator is composed of multiple layers with in-plane magnetic anisotropy[80]. In this particular case, the Dirac cone shifts from the Γ point of the surface Brillouin zone along the direction perpendicular to the magnetic moment without opening a

Fermi arcs
Disconnected arcs in momentum space appearing at the surface of certain materials such as Weyl semimetals.

Topological magnetoelectric effect
Generation of a quantized contribution to the magnetization by applying an external electric field.

mass gap[79,80]. This can also be described within the BR model with an external field (BOX 2). Recently, a number of in-plane magnetized semiconductors — $MnBi_2Te_2Se_2$, VBi_2Se_4, $VBi_2Te_2Se_2$, VBi_2Te_4, $VSb_2Te_2Se_2$ and VSb_2Te_4 — with Néel temperature in the range 77–94 K have been proposed as antiferromagnetic topological insulators[80]. An especially interesting electronic feature — a topological 1D flat electron state — emerges in such systems at linear domain walls, giving rise to a sharp peak in the density of states peak near the Fermi level[80,81]. This state, being polarized out-of-plane, can be effectively tuned by applying an external magnetic field perpendicular to the surface plane.

Extension of topological theory to magnetic WSMs can greatly increase the number of ferro- and antiferromagnetic systems that can be used in the search for new quantum phenomena. There have already been a number of magnetic WSMs predicted and partly studied, such as Co-based Heusler half-metals XCo_2Y (with X from groups IVB or VB, Y from IVA or IIIA)[99], $Co_3Sn_2S_2$ (REF.[100]), Mn_3Sn, Mn_3Ge (REFS.[101,102]) and some others. Especially intriguing are antiferromagnetic WSMs which, in contrast to normal antiferromagnets, demonstrate strong anomalous Hall transport due to the existence of Weyl nodes. Recent discovery of the correlated magnetic Weyl semimetal with logarithmic Fermi velocity renormalization in strained pyrochlore iridate $Pr_2Ir_2O_7$ demonstrates a huge potential for combinations of electron correlations with strain, magnetism and topology for development of new magnetically active WSMs[103].

Rashba effect in strongly correlated materials

4f compounds. Spin–orbit coupling plays an essential role in the development of new quantum materials with strong electron correlations. At the heart of such systems are the 4*f* compounds, which constantly attract attention due to their exotic bulk properties. Among these properties are complex magnetic phases, unconventional superconductivity including non-centrosymmetric superconductivity, heavy-fermion behaviour, Kondo physics, quantum criticality, valence fluctuations and skyrmion lattices[104–107]. Now, the surfaces and interfaces of 4*f* systems are increasingly moving into the focus of interest, as versatile 2D platforms for studying the influence of inversion symmetry breaking and Rashba spin–orbit coupling on the exotic properties of the strongly correlated *f* states[23,24,108–113].

An illustrative example is the family of RET_2Si_2 materials, where RE is a rare-earth and T is a transition metal atom[108,109]. Depending on composition, RET_2Si_2 systems show prominent *f*-driven properties. Their layered structure, where RE atomic planes are separated by silicide Si–T–Si blocks, allows easy cleaving of the sample and obtaining surfaces with a mosaic of usually large REs and silicide (Si–T–Si–RE) terminations[110,111]. Note that their electronic structure and temperatures scales are remarkably different from each other and from those in the bulk[114]. The strength of the spin–orbit coupling can be tuned by exchanging the transition metal: the strength increases on going from Co to Rh and further to Ir. To trigger an interplay with the Rashba spin–orbit coupling, one may introduce magnetic exchange interaction by inserting elementary 4*f* magnets such as Gd and consider the Si–Rh(Ir)–Si–Gd surface[111,115]. As the orbital moment of the Gd 4*f* shell is equal to zero, this makes it insensitive to the crystal field. Selecting REs with non-vanishing 4*f* orbital moment, such as Ho, Dy or Tb, leads to rotation of the respective 4*f* moments to certain angles relative to the surface normal, caused by their coupling to the crystal field[24,109]. This allows for creating an exchange field near the surface with different strengths and orientations, and enables the exploration of how 2D carriers behave in the presence of competing Rashba and magnetic exchange fields. By choosing Ce or Yb as the RE element, one may explore how the emergent Kondo physics and heavy-fermion properties will be affected by the Rashba spin–orbit coupling[108].

The silicide surfaces of RET_2Si_2 are characterized by strongly dispersive surface states residing in a large projected $\overline{M}$-gap. The surface states reveal distinct orbital compositions and localizations. Their rather different spin structures are governed by the conventional and cubic Rashba effects[24,109–111,115]. In the latter case, the electron spin reveals three complete rotations upon moving once around the constant energy contours[24,110,111] (FIG. 4). To investigate how such exotic spin properties would change when magnetic order sets in, one can consider the iridium silicide surfaces of antiferromagnetic $GdIr_2Si_2$ and valence-fluctuating $EuIr_2Si_2$ (REFS.[110,111]). The beauty of $EuIr_2Si_2$ is that this material is non-magnetic in the bulk, owing to a mixed-valent state of Eu. However, the first Eu layer buried by the surface iridium silicide block behaves divalently and acts as a source of 2D ferromagnetism[110,114]. FIGURE 4 shows how the rotational symmetry of the $\overline{M}$ surface state is reduced when the 2D ferromagnetism from this single Eu layer sets in. Red arrows indicate the points in k space between which the electron spin rotates by 2π owing to the cubic Rashba effect[110].

Another intriguing property of the surface states is that their in-plane spin structure governed by Rashba spin–orbit coupling survives and remains intact when the material transfers to the antiferromagnetic regime, as was shown for $TbRh_2Si_2$ (REF.[24]). A substitution of Rh by Ir and Tb by Yb brings us to the heavy-fermion material $YbIr_2Si_2$ (REF.[108]). On its iridium silicide Si–Ir–Si–Yb surface, Rashba spin–orbit coupling induces spin polarization of the 2D electrons, while a hidden layer of Yb 4*f* moments acts as a source for coherent *f*–*d* interaction. Analysis of the fine 4*f*-derived spectral pattern suggests that the spin–orbit coupling also leads to the narrow spin splittings of the 4*f*-heavy bands[108]. Exploiting the combination of Kondo and Rashba physics in the non-centrosymmetric 4*f* systems opens new opportunities to handle the 2D itinerant and 4*f*-hybrid states as their spin properties and group velocities offer new functionalities.

Similarly to the discussed RET_2Si_2 materials, the surfaces and interfaces as well as multilayer sequences of other families of *f* systems have also received attention[116–118]. Recently, for heavy-fermion superconductor $CeIrIn_5$, the strong Rashba effect and, as a consequence, the heavy linearly dispersing spin-split surface states

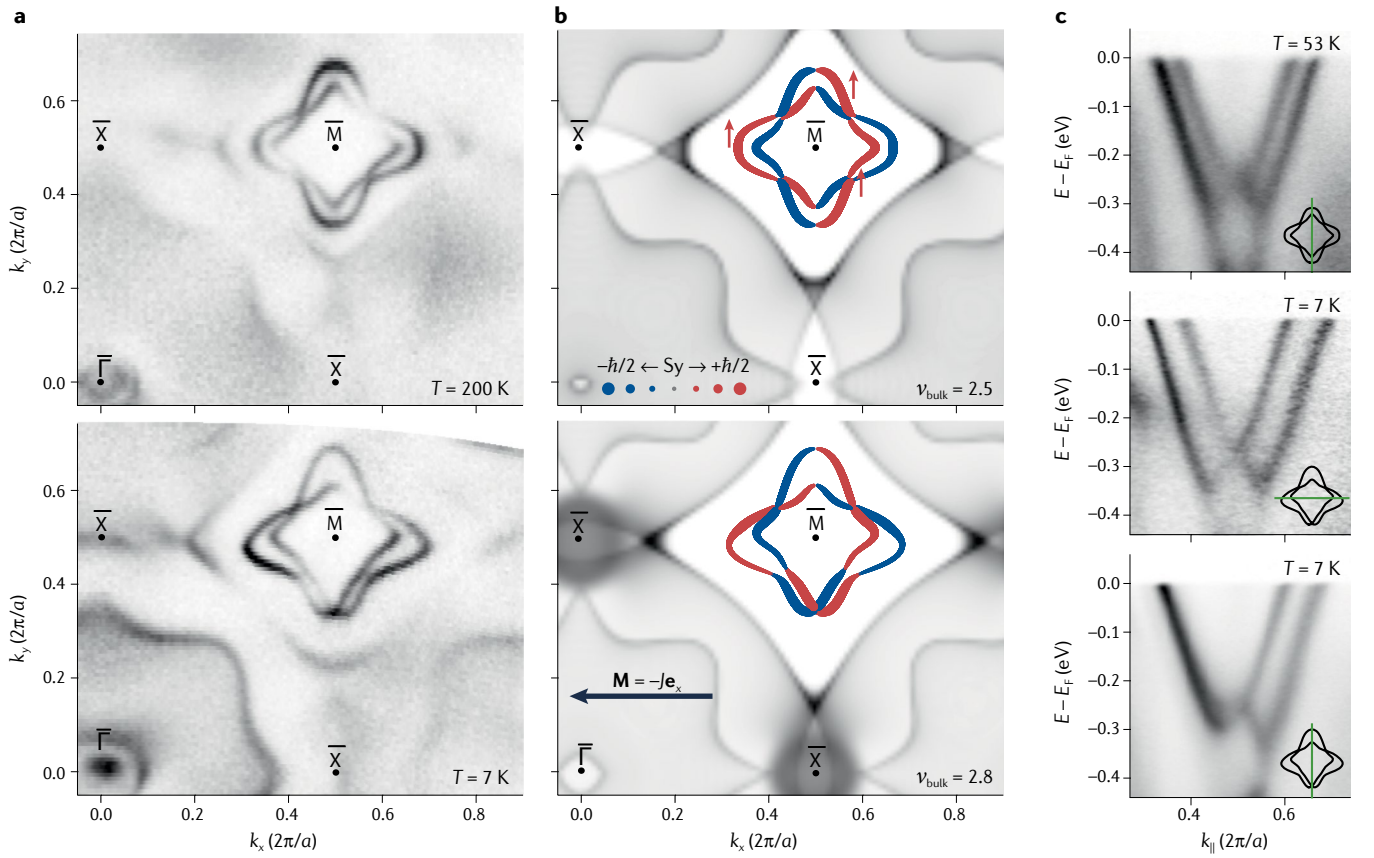

Fig. 4 | **Cubic Rashba effect and emergence of 2D ferromagnetism at iridium silicide surface of valence-fluctuating $EuIr_2Si_2$. a** | Fermi surface at 200 K (upper panel) and 7 K (lower panel). The results are derived from angle-resolved photoemission spectroscopy (ARPES). **b** | The computed Fermi surface for 200 K (upper panel) and 7 K (lower panel), shown as a superposition of projected bulk and slab-derived states calculated within density functional theory. The surface state is highlighted by the spin expectation value S_y in red ($S_y > 0$) and blue ($S_y < 0$). The black arrow indicates the direction of the emergent magnetic field. **M** denotes the magnetization, J reflects the strength of exchange interaction and $\mathbf{e}_x$ is a unit vector along the x-axis. **c** | ARPES patterns showing modifications of surface state dispersion when 2D ferromagnetism emerges at low temperature. Insets indicate the respective cuts through the Fermi surface. Figure adapted with permission from REF.[110] under a Creative Commons licence CC BY 4.0.

at the CeIn surface were predicted theoretically and unveiled in ARPES experiments[116]. Note that quasi-2D $CeIrIn_5$ belongs to a larger family of $Ce_nT_mIn_{3n+2m}$ correlated materials, where T = Co, Rh, Ir, Pd and Pt. Then one can argue that, at the surfaces of such systems, similar or more advanced properties as well as new temperature scales can be anticipated, owing to the joint presence and possible synergy of *f*-driven phenomena and phenomena related to Rashba spin–orbit coupling. Another noticeable example is superconducting superlattices, which contain alternating blocks of the heavy-fermion superconductor $CeCoIn_5$ with fixed thickness and non-magnetic metal $YbCoIn_5$ with variable thicknesses[118]. As an example of such artificially engineered superlattices, it was suggested that tunable Rashba spin–orbit coupling in $CeCoIn_5$ blocks influences the Pauli pair-breaking effect[118].

Non-centrosymmetric superconductors. In conventional superconductors, the ground state is composed of spin-singlet Cooper pairs. A decade ago, it was realized that injecting spin-polarized currents in superconductors could achieve long-lived spin-triplet quasiparticle currents[119], a prerequisite for superconducting spintronics[120–123]. Alternatively, Rashba spin–orbit coupling in non-centrosymmetric superconductors or at their interface may also aid the formation of long-ranged spin triplets. In a nutshell, the Rashba spin–momentum locking near Fermi level leads to a mixing of the pairing parity[124,125]. As a result, in non-centrosymmetric superconductors there is neither separation according to parity nor spin-singlet and spin-triplet pairing, and the superconducting state represents a mixture of singlet and triplet pair states[107].

The classical examples are Ce-based heavy-fermion non-centrosymmetric superconductors such as $CePt_3Si$, $CeIrSi_3$ and $CeRhSi_3$ (REFS.[107,126]). Owing to the delicate interplay between *f* and *d* electrons, such systems reveal rich magnetic and superconducting properties, where the latter are most probably governed by spin fluctuations originating from *f* states. Another class of non-centrosymmetric superconducting materials that do not contain the magnetically active *f* states encompasses $LaNiC_2$, La_7Ir_3, Zr_3Ir, CaPtAs and ReT. The superconductivity of these materials seems not to be mediated by the spin fluctuations, and the intrinsic pairing mechanism is being actively investigated[125]. In some weakly correlated non-centrosymmetric superconductors, the

Pairing parity
Symmetry property describing the behaviour of the wavefunction of a Cooper pair under permutation of the paired electrons.

muon-spin relaxation technique has recently unveiled superconductivity with broken time-reversal symmetry, which remains a hot topic[125]. As far as *f* systems are concerned, we wish to mention the freshly discovered material $CeRh_2As_2$ which reveals two distinct superconducting phases[127]. A transition between these phases occurs when an external magnetic field is applied along a specific direction. Although many open questions remain about the precise nature of the superconducting mechanism in this material, it is suggested that local inversion symmetry breaking at the cerium sites leads to Rashba-like spin–orbit coupling, which is likely to play a decisive role for multiphase superconducting properties[127]. Thus, the topic of non-centrosymmetric superconductors remains hot for both strongly and weakly correlated electron systems, with and without *f* states.

As mentioned above, Rashba spin–orbit coupling is also a central ingredient for the realization of synthetic topological superconductors and the observation of Majorana bound states. A popular proposal[59,60] consists of bringing a nanowire with strong Rashba spin–orbit coupling in proximity to an *s*-wave superconductor. In the presence of external magnetic field, tuning the chemical potential in the gap of the band structure leads to the emergence of Majorana bound states at the ends of the nanowire[61,128] (for further discussion, see REF.[129]).

Box 3 | **The Edelstein effect**

The direct Edelstein effect (DEE) and the inverse Edelstein effect (IEE) are related to the shift of the Fermi contour associated with the charge and spin current injection. As depicted in panel **a**, injecting a 2D charge current $\mathbf{J}_c^{2D}$ along *x* leads to a shift $\Delta\mathbf{k}$ of the contours and to an out-of-equilibrium spin population **S** along *y*. If this spin accumulation can relax to an adjacent material, a 3D spin current $\mathbf{J}_s^{3D}$ will flow. Reciprocally, the injection of a 3D spin current $\mathbf{J}_s^{3D}$ with spin along *y* as shown in panel **b** leads to a shift of the contours $\Delta\mathbf{k}$, and to an out-of-equilibrium charge population and a 2D charge current $\mathbf{J}_c^{2D}$ along *x* in the Rashba material.

The figures of merit of the conversion efficiencies are $q_{DEE} = J_s^{3D}/J_c^{2D}$ in m^{-1} for the DEE and $\lambda_{IEE} = J_c^{2D}/J_s^{3D}$ in m for the IEE. To compare them with the spin Hall angle Θ_{SHE} in the SHE case, it was proposed to compare the maximum ratio for the conversion obtained after integrating the 3D current in the SHE case into an equivalent 2*D* surface current[145]. This leads to the following relations: $q_{DEE} = 0.38\Theta_{SHE}/\lambda_s$ and $\lambda_{IEE} = \Theta_{SHE}\lambda_s$ with λ_s the spin diffusion length of the SHE material corresponding to the effective 3D thickness.

As the DEE and IEE are out-of-equilibrium effects, the conversion efficiency depends on the spin relaxation times[146,168–170]. In the DEE case, a large out-of-equilibrium spin accumulation and a short spin transmission time across the interface τ_t leads to a large spin current J_s^{3D}. For the IEE, a long spin relaxation time in the Rashba states τ_R and spin transmission time across the interface maximize the shift of the contour and the spin-to-charge current conversion efficiency. Following the phenomenological model of REF.[169], the conversion efficiencies can be written

$$q_{DEE} \propto \frac{\alpha_R}{v_F^2 \hbar \tau_t}, \quad \lambda_{IEE} \propto \frac{\alpha_R}{\hbar}\frac{\tau_p \tau_t}{\tau_p + \tau_t}, \tag{6}$$

with α_R the Rashba constant and v_F the Fermi velocity of the Rashba system. IEE and DEE are therefore maximized for a large Rashba constant but for different relaxation times. Optimization of the conversion is possible for each conversion direction but not for both at the same time.

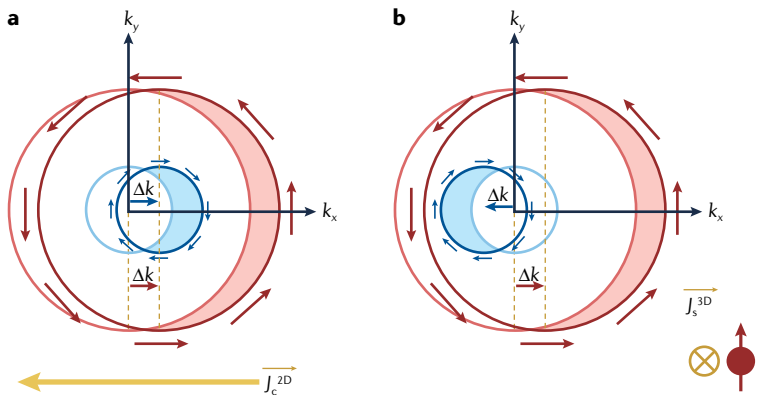

Non-equilibrium Rashba effects

Spin–charge interconversion

The spin–momentum locking associated with the Rashba spin splitting promotes the interconversion between electron flows and pure spin flows (and reciprocally, the interconversion of pure spin flows into electron flows), enabling current-driven spin–orbit torque[130–132], magnetic state readout[133] and laser-induced terahertz (THz) emission[134]. The idea that Rashba systems could support the conversion of a charge flow into a spin density was originally proposed and reported in non-centrosymmetric semiconductors[135–138], an effect known as the inverse spin galvanic effect or the direct Edelstein effect (DEE). Its Onsager reciprocal, the spin-to-charge interconversion[135,139,140], is called the spin galvanic effect or the inverse Edelstein effect (IEE). In the following, we will use this latter terminology for simplicity. In recent years, numerous Rashba-related systems offering efficient spin-charge interconversion through the Edelstein effect have been proposed. As DEE is associated with the spin–momentum locking, it also occurs at the surface states of 3D topological insulators[141] and Weyl semimetals[142], and is not limited to systems described by the Rashba Hamiltonian.

In metallic heterostructures, the (direct and inverse) Edelstein effect usually coexists with (direct and inverse) SHE, a mechanism present in the bulk of heavy metals that also induces spin-charge interconversion[143]. Despite their different physical origin, DEE-driven and SHE-driven interconversions lead to similar outcomes, making the two contributions difficult to disentangle[144]. The key difference between them is their dimensionality. The SHE (inverse SHE) converts a 3D charge (spin) current into a 3D spin (charge) current; the figure of merit of the conversion, the spin Hall angle Θ_{SHE}, is dimensionless. In contrast, the DEE (IEE) converts a 2D charge (spin) current into a 3D spin (charge) current; the figure of merit is therefore the inverse of a length q_{DEE} and λ_{IEE} (BOX 3)[145].

The signature of a large spin-to-charge conversion via IEE was reported at the Bi/Ag interface, which possesses a large Rashba coefficient α_R of 3.05 eV Å (REF.[12]). Using the spin-pumping method, where a magnetization precessing at ferromagnetic resonance injects a spin current in an adjacent metallic layer, a spin-to-charge conversion efficiency of 0.3 nm was obtained in NiFe/Ag/Bi, similar to the conversion in NiFe/Pt (REF.[146]). The spin–charge interconversion in the Bi/Ag bilayer was further evidenced by various techniques[147–150] and at similar interfaces such as Ag/Sb (REF.[151]) or Ag/Bi_2O_3 (REF.[152]). As IEE switches sign on inversion of the stacking order, whereas SHE is insensitive to it, by inverting the stacking order in Bi/Ag it is possible to test the physical origin of the

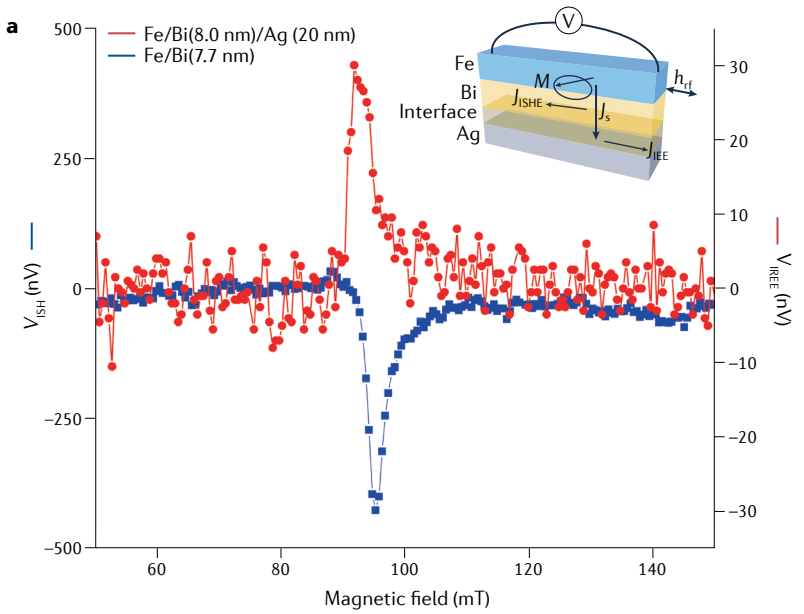

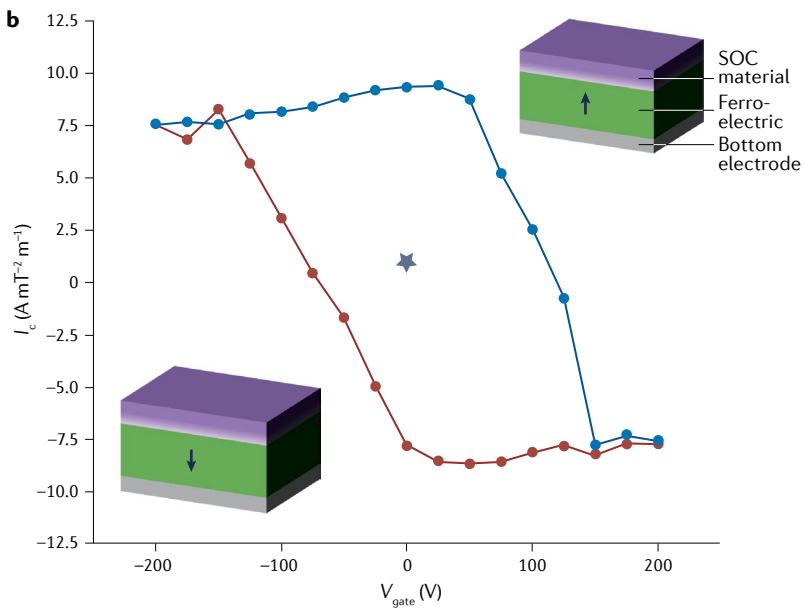

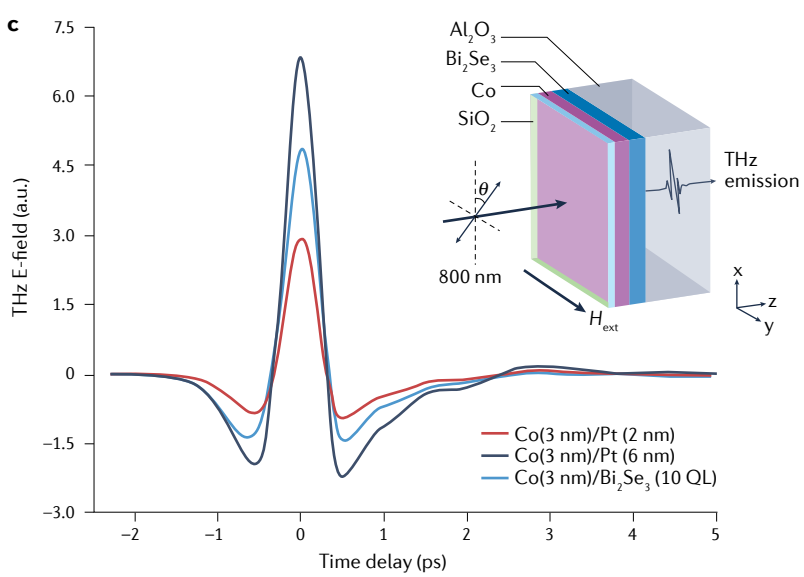

Fig. 5 | **Spin–charge interconversion using the Rashba effect. a** | Measured spin-pumping signal for Bi(7.7 nm)/Fe and Ag(20 nm)/Bi(8.0 nm)/Fe stacks at positive magnetic fields with a schematic illustration of the spin-pumping ferromagnetic resonance (FMR) measurement. Upon FMR, a spin current J_s is injected toward the Ag/Bi interface and converted via the inverse spin Hall effect and the inverse Edelstein effect. The sign of the signal at FMR is reversed in the sample with Ag capping. **b** | Gate-voltage dependence of the normalized current produced by the inverse Edelstein effect using spin-pumping FMR in a NiFe (20 nm)/Al(0.9 nm)/$SrTiO_3$ exhibiting remanence. The inset shows a sketch of the polarization state corresponding to each remanent state. **c** | Schematic illustration of THz emission from Bi_2Se_3/Co heterostructure. The sample is excited by femtosecond laser pulses, and the electric field of the emitted THz pulse is then detected using electro-optic sampling (left). The THz emission from Bi_2Se_3 (10 QL)/Co (3 nm) is comparable to that in highly efficient Pt/Co emitters (right). SOC, spin–orbit coupling; QL, quintuple layer. Panel **a** adapted with permission from REF.[153], AIP. Panel **b** adapted with permission from REF.[174], Springer Nature Ltd. Panel **c** adapted with permission from REF.[179], Wiley.

interconversion. Because of the importance of the stacking order in the present discussion, we use the following convention to describe the heterostructures: top/middle/bottom layer. An opposite sign of the spin-pumping signal in Bi/Ag/Fe and Bi/Fe was observed[153] (FIG. 5a). Although the sign inversion was observed by others[147,154] in the same systems, the exact nature of the conversion remains controversial. This is due to the difficulty of growing an inverted structure with identical interface quality and properties, which can be affected by alloying[155,156], and the large difference between the spin diffusion length of Ag and Bi, requiring thin Bi films[151].

In a free-electron model (BOX 3), Rashba spin–orbit coupling splits the Fermi surface into two contours of opposite helicities that partially compensate each other, resulting in a reduction of the interconversion efficiency. With this simple rule of thumb, the surface states of 3D topological insulators with Dirac-like spin–momentum locking and only one helicity should therefore be optimal to obtain efficient conversion from the DEE effect. In 2014, a large spin Hall angle of 350% in Py/Bi_2Se_3 was obtained, one order of magnitude larger than in the best heavy metals[157]. The same year, current-induced magnetization switching was reported in a magnetically doped topological insulator heterostructure $(Bi_{0.5}Sb_{0.5})_2Te_3$/$(Cr_{0.08}Bi_{0.54}Sb_{0.38})_2Te_3$ with a low critical current density of 8.9×10^4 A cm^{-2} at 1.9 K, orders of magnitude lower than in the best heavy metals[158]. The very large charge-to-spin conversion efficiency in topological insulators heterostructures was further evidenced, including the possibility of obtaining low-current-density magnetization switching at room temperature[159–161]. The origin of the torque is usually ascribed to the spin–momentum locking of the surface states, although properly separating the multiple contributions to the interconversion is still an unresolved experimental and theoretical challenge owing to additional bulk contribution (such as SHE), alloying or interfacial Rashba states[162]. For extensive reviews of the recent results on spin–orbit torque in topological insulators, see elsewhere[132,163].

Noticeably, the reciprocal conversion from spin-to-charge in topological insulators is smaller than in heavy metals or at the Bi/Ag interface, with values of the IEE length below 0.1 nm (REFS.[164–166]). Only a few efficient spin-to-charge conversion results were reported in non-van-der-Waals systems like α-Sn (REF.[167]). This apparent discrepancy is likely to be due to the different sensitivity of the DEE and IEE to the transport relaxation times[168,169] (BOX 3). The largest spin-to-charge conversion efficiencies are reported in the 2D electron gases $LaAlO_3/SrTiO_3$ and $AlOx/SrTiO_3$ at cryogenic temperature[170–172]. While the Rashba coefficient in the conduction band of $SrTiO_3$ is two orders of magnitude smaller than in Bi/Ag, with a maximum α_R of 40 meV Å (REF.[173]), the spin-to-charge conversion is larger thanks to the high carrier mobility and the long interface transmission time through the oxide overlayer $LaAlO_3$ and $AlOx_x$. With λ_{IEE} ranging from 3 nm to 30 nm at cryogenic temperature, the spin relaxation times are of the order of a picosecond in oxides whereas they are only a few femtoseconds in metallic interfaces[146,170]. An additional interesting feature of this system is the possibility of tuning the Fermi level position with a back gate and modulating the conversion efficiency, which is maximum at specific points of the band structure[171]. Below 34 K, in the field-induced ferroelectric phase of $SrTiO_3$, the gate control of the 2D electron gas is hysteretic. By changing the electric polarization of the $SrTiO_3$ crystal with a back gate, remanent control of the amplitude and sign of the spin-charge conversion in NiFe/Al/ $SrTiO_3$ is obtained[174], offering new possibilities for the control of the Edelstein effect and for logic applications (FIG. 5b). Ferroelectric Rashba semiconductors such as GeTe in which the helicity of the Rashba contour can be controlled via the electric polarization[16] were also recently shown to offer similar control at room temperature[175].

Despite a large spin–charge interconversion, the high resistivity of most topological insulators and Rashba interfaces is detrimental for low-power non-volatile memory applications[176]. In parallel with the development of materials with lower resistivity such as BiSb (REF.[177]), new concepts have been proposed. The magnetoelectric spin–orbit logic, recently proposed by Intel as being scalable beyond CMOS logic, scales favourably with the resistivity and spin-to-charge conversion efficiency[178]. Highly efficient spintronic THz emitters outperforming other available systems at lower cost were recently demonstrated in heavy metal systems Pt/CoFeB (REF.[134]). Femtosecond laser pulses were used to drive THz emission in a Bi_2Se_3/Co bilayer (FIG. 5c); the amplitude of the THz emission obtained is similar to that of the highly efficient Pt/Co system[179]. These new concepts offer a variety of possible applications for Rashba systems.

Nonlinear transport properties

The interplay between antisymmetric spin–momentum locking due to Rashba-like interaction and time-reversal-symmetry breaking results in non-reciprocal transport at the second order in electric field. In other words, the resistivity of the system acquires a term that is linear in both the electric and the magnetic fields, such that $\rho = \Sigma_{ij}\gamma_{ij}B_iE_j$. In magnetic systems, similar effects proportional to both the electric field and magnetization direction will emerge. The form of the tensorial response γ_{ij} is dictated by the spatial symmetries of the system. This effect is sometimes referred to as a 'magnetoelectric rectification' effect in analogy with electrooptical rectification, where a DC response is obtained at the second order of the AC excitation. Note that because these magnetochiral effects have been investigated by researchers from different disciplines, using different experimental techniques and focusing on different classes of materials, no formal consensus has been adopted regarding the nomenclature of these effects. Hence, when reading the literature, one often encounters different denominations for fundamentally similar effects. We do not attempt to reconcile these different views here, and rather focus on providing an overview of the state-of-the-art.

Magnetoelectric rectification was originally proposed in Si field-effect transistors submitted to an external magnetic field and called electrical magnetochiral anisotropy[180]. In this case, the magnetic field is applied along the electric current. This effect is also observed in bulk chiral molecular conductors[181]. This effect has recently been extended to non-centrosymmetric non-magnetic materials such as BiTeBr (REF.[182]) and α-GeTe, both materials possessing a strong bulk Rashba effect, to Ge(111) (REF.[183]) and to $LaAlO_3/SrTiO_3$ interfaces[173,184]. In the latter, the effect can be modulated by a gate voltage. In these non-magnetic systems, the rectification effect reveals itself as a unidirectional magnetoresistance; that is, a resistive contribution of the form $\rho \propto \mathbf{B}\cdot(\mathbf{z}\times\mathbf{I})$, where $\mathbf{I}$ is the injected current. This form arises from the competition between Zeeman exchange and the current-driven Rashba field (DEE). We emphasize that although the rectification effect is rather robust, its particular tensorial form (γ_{ij}) and the underlying mechanisms contributing to it depend on the specifics of the spin texture in momentum space and on crystal symmetries. For instance, in Bi_2Se_3 topological insulator surfaces[185], an additional angular dependence of the unidirectional magnetoresistance reflects the existence of three-fold anisotropy of the Fermi surface (trigonal warping) as well as out-of-plane spin texture. Similarly, WTe_2 displays an anisotropic unidirectional magnetoresistance that correlates with the crystal symmetries, and an inversion of the sign of the signal is associated with the distortion of the Fermi surface of WTe_2 (REF.[186]). Similar effects have been observed in superconductors such as Bi_2Te_3/FeTe (REF.[187]), $PbTaSe_2$ (REF.[188]) and $SrTiO_3$ (REF.[189]), with an enhancement below the superconducting transition. Note that the unidirectional magnetoresistance is associated with a nonlinear planar Hall effect[190], an effect that remains to be further understood.

The unidirectional magnetoresistance has also been reported in magnetic systems, where the external magnetic field $\mathbf{B}$ is replaced by magnetization $\mathbf{M}$. In these situations, the resistivity is odd in magnetization and adopts similar symmetry, $\rho \propto \mathbf{M}\cdot(\mathbf{z}\times\mathrm{I})$, as exposed above. The effect has been reported in GaMnAs (REF.[191]) and NiMnSb (REF.[192]), but also in heterostructures made out of a ferromagnet deposited on a heavy transition metal[193] or a topological insulator substrate[194,195]. Owing to the interplay between spin–orbit coupling and magnetism, the underlying mechanisms are diverse, involve

Non-reciprocal transport
Inequivalence of the conductivity of a material or a heterostructure upon changing the current polarity.

Nonlinear anomalous Hall effect
Charge current flowing transverse to the injected current in the absence of time-reversal symmetry breaking and at second order in the electric field.

complex spin scattering effects, possibly SHE, and can involve electron–magnon interaction[196].

Another important effect that has been uncovered in non-centrosymmetric materials is the nonlinear anomalous Hall effect, which is second order in electric field. This effect is particularly intriguing because unlike the linear (ordinary or anomalous) Hall effect that requires time-reversal symmetry breaking, the nonlinear Hall effect exists even in non-magnetic non-centrosymmetric systems in the absence of an external magnetic field. Although not a direct consequence of Rashba spin–orbit coupling, this effect necessitates inversion symmetry breaking and is therefore of interest for the present Review. The nonlinear Hall effect has been reported recently in non-magnetic Weyl semimetals, for example WTe_2 (REFS.[197,198]), $TaIrTe_4$ (REF.[199]) and more recently $Ce_3Bi_4Pd_3$ (REF.[200]). From the microscopic standpoint, the nonlinear Hall effect is a consequence of the dipole moment of the Berry curvature[201,202]. The nonlinear Hall effect is particularly interesting as it offers opportunities for the rectification of radiofrequency[199] or THz electric fields[203].

Optoelectronics mediated by Rashba effect

The optical response of non-centrosymmetric materials is remarkably rich and goes far beyond the specific case of Rashba-like systems. In particular, breaking both the inversion symmetry and time-reversal symmetry leads to non-reciprocal optical activity such as directional dichroism and birefringence, as observed in multiferroics, as well as second-harmonic generation and nonlinear Kerr rotation. We do not intend to provide a broad description of these effects as they are not specific to Rashba-like interaction, and invite the reader to refer to specialized reviews[204,205]. Instead, we focus on two optical effects that have been originally observed in Rashba systems and recently extended to other non-centrosymmetric compounds.

Non-centrosymmetric materials are known to display the photogalvanic effect. For linearly polarized light, the induced charge current is associated with a shift in the real-space position of the electron wavepacket during light-induced interband transition. This 'shift current' is associated with the Berry connection and has been reported in a wide range of ferroelectrics[206–208]. In the case of circularly polarized light, the mechanism underlying the photogalvanic effect is different. The circularly polarized light excites a non-equilibrium spin density via spin-selective transition which, via the antisymmetric spin–momentum locking induced by the Rashba effect, can be converted into a DC charge current. This is the optical analogue of IEE discussed previously. This effect[135] was reported in Te in the 1970s[136] and later in n-GaAs/AlGaAs quantum wells[140]. More recently, the photogalvanic effect has also been reported at the surface of topological insulators, where Dirac states are present[209–211]. As already mentioned, it remains unclear whether the photocurrent collected at these surfaces can be solely ascribed to topological surface Dirac states or whether trivial Rashba states also contribute.

Another domain in which Rashba spin–orbit coupling can substantially affect optical properties concerns hybrid perovskite solar cells[212,213]. In fact, hybrid perovskites possess a heavy metal element that can promote large Rashba spin splitting in the band structure[214,215]. Hence, it has been proposed that this feature could be responsible for the long recombination time observed in these materials[216]. Rashba spin splitting introduces two key features in the band structure: a shift of the band extrema in momentum space and a spin texture. If the momentum shift and/or the spin texture of the conduction and valence bands differ significantly, one can expect a suppression of radiative recombination of the exciton. The idea has attracted substantial interest, and several studies have aimed to specifically identify the role of Rashba spin–orbit coupling on the electron–hole recombination rate, but this question remains open.

Optical manipulation of Rashba spin splitting

At interfaces[217] and in ferroelectric materials such as GeTe (REF.[16]), the magnitude of Rashba spin splitting can be manipulated by using an electrical gate. Conversely, the strength of the spin–momentum locking can also be manipulated using optical gating. In one work[218], the authors consider $SrTiO_3$, an insulator with conducting surface states that display sizable Rashba spin–orbit coupling. Electrons occupying in-gap states associated with oxygen vacancies are optically excited to the conduction band and diffuse towards the surface where they are trapped in the potential well. These additional charges modify the potential profile and thereby the Rashba strength. Such an all-optical modulation of Rashba spin splitting was also achieved recently at the surface of Bi_2Se_3 (REF.[219]), where the optical excitation triggers a charge redistribution close to the interface inducing an ultrafast photovoltage. This photovoltage modifies the band bending close to the surface and thereby the Rashba strength.

Besides optical gating, another effect arises when light is shone on an electron gas. When a quantum system is periodically driven by an electromagnetic excitation, the eigenstates are described by Floquet states, the analogue of Bloch states for time-periodic systems. In other words, when an electron gas is illuminated by high frequency light, the carriers become 'dressed' by the electromagnetic field, and their energy dispersion is modified. The effect is particularly spectacular in the case of a spin–orbit coupled system since the electromagnetic field couples directly to the spin degree of freedom via its vector potential: $\boldsymbol{\sigma}\cdot(\mathbf{p}\times\mathbf{z})\rightarrow\boldsymbol{\sigma}\cdot[(\mathbf{p}+e\mathbf{A})\times\mathbf{z}]$. This unique coupling can therefore strongly modify the band structure of Rashba-type systems. In particular, it can drive topological phase transition in quantum wells[220], open orbital gaps at the surface of topological insulators[221], or even induce the anomalous Hall effect in (centrosymmetric and spin–orbit free) Dirac semimetals such as graphene[222]. We emphasize that to the best of our knowledge, the research on Floquet engineering of more conventional Rashba physics remains poorly explored[223].

Perspectives

The physics unlocked by the spin–orbit coupling in materials lacking a centre of inversion has led to remarkable discoveries in the past 60 years, motivated not only by the numerous puzzling effects it encompasses (electric dipole spin resonance, anisotropic spin relaxation and

persistent spin spirals, spin galvanic effect, Aharonov–Casher effect and so on), but also by the potentially disruptive applications it enables[1,2]. Initially limited to semiconducting quantum wells and bulk materials, where the Rashba and Dresselhaus spin–orbit coupling can be finely controlled, this research has recently been extended to new classes of materials with much more unconventional spin–momentum locking schemes. The fundamental understanding of spin transport acquired from investigations along these lines has greatly contributed to the blooming of topological materials. In the past 10 years, a diverse landscape of transport phenomena has started to emerge in the linear regime and beyond. However, several questions remain open in the short and longer term.

Short-term questions

So far, the largest Rashba parameters reported at Bi/Ag(111) (REF.[12]) and Bi_2Se_3 (REF.[224]) surfaces and in bulk BiTeI (REF.[14]) do not exceed 4 eV Å. Clear guiding principles need to be established for the design of bulk materials or heterostructures displaying maximal Rashba-like spin–momentum locking. Although it is clear that this unique spin–momentum locking arises from the competition between atomic spin–orbit coupling and the potential drop associated with the (bulk or interfacial) inversion symmetry breaking, a quantitative, high-level theory that can inspire a robust strategy to enhance the strength of the Rashba-like spin–momentum locking is highly desirable.

Materials possessing large Rashba-like spin–orbit coupling tend to display not only large spin-to-charge conversion, but also short spin relaxation time, which is in turn detrimental to the overall conversion efficiency. A compromise between these two effects is necessary to boost the device performance.

Although high-throughput first-principles simulations have accelerated the prediction of new materials with unconventional electronic properties[225–229], their experimental realization remains a challenge. This is particularly true for topological insulators, semimetals and strongly correlated materials, which have the potential to display extremely large Rashba-like behaviour, as discussed in this Review. Besides these exotic candidates, 2D van der Waals materials present a promising opportunity for nanoscale engineering of Rashba-like spin–momentum locking by stacking different monolayers[27] or using Janus configuration at the level of a single monolayer[31,32]. Finally, a particularly inspiring research direction concerns strongly correlated materials (including the topological ones) involving either 4*f* or 5*f* elements and whose surface states host exotic properties that remain to be identified and characterized.

In heterostructures, interfacial Rashba-like interaction often coexists with spin–orbit coupling from the materials' bulk. The latter generates several mechanisms that interconnect spin currents with charge flow, including, but not limited to, SHE. In spin-to-charge conversion experiments, it is therefore often difficult to distinguish between these two microscopic origins. A similar issue arises at the surface of topological materials, where topological Dirac states might coexist with trivial Rashba-like states. In both cases, identifying efficient means to characterize the microscopic origin of the observed effects is a crucial step towards their optimal control.

Long-term challenges

So far, transport properties associated with Rashba-like spin–orbit interaction have been mostly studied in the DC regime. In fact, as the energy associated with spin–orbit coupling is typically a few tens of meV, one can expect spin dynamics in the THz regime. The unique Rashba spin–momentum locking can promote the Zitterbewegung effect (the jittering motion of spin-polarized wave packets)[230], which to the best of our knowledge has not been reported in condensed matter, as well as ultrafast spin-to-charge conversion leading to high-harmonic generation as suggested recently[231,232].

Nonlinear effects such as unidirectional magnetoresistance and the nonlinear Hall effect are currently attracting a massive amount of interest, as they can be used to probe otherwise-invisible magnetic order[233] or to detect THz signals[203]. The search for materials with enhanced nonlinear response and the exploration of the mechanisms that sustain them should open new avenues.

A research direction that can potentially bring entirely new ideas to condensed matter physics is the realization of a Rashba-like spin–momentum locking scheme in the absence of spin–orbit coupling. Such schemes can be achieved in non-centrosymmetric non-collinear magnets[56]. Along similar lines, the possibility of designing an orbital-momentum locking scheme opens fascinating perspectives for pure orbitronics[44,47,48].

Finally, beyond condensed matter physics, the concept of Rashba-like spin–orbit coupling has been successfully extended to cold atoms, where synthetic spin–orbit coupling can be implemented, leading to exotic realization of Rashba-like physics[234]. Other new classes of systems in which Rashba-like physics would be worth investigating are non-Hermitian systems[235], where the combination of parity and time is preserved, and topolectrical circuits[236], in which solid state materials are modelled using conventional electrical circuits.

Published online: 24 August 2022

1. Manchon, A., Koo, H. C., Nitta, J., Frolov, S. M. & Duine, R. A. New perspectives for Rashba spin–orbit coupling. *Nat. Mater.* **14**, 871–882 (2015).
2. Bihlmayer, G., Rader, O. & Winkler, R. Focus on the Rashba effect. *New J. Phys.* **17**, 050202 (2015).
3. Yeom, H. W. & Grioni, M. Special issue on electron spectroscopy for Rashba spin–orbit interaction. *J. Electron Spectros. Relat. Phenomena* **201**, 1–126 (2015).
4. LaShell, S., McDougall, B. A. & Jensen, E. Spin splitting of an Au(111) surface state band observed with angle resolved photoelectron spectroscopy. *Phys. Rev. Lett.* **77**, 3419–3422 (1996).
5. Hoesch, M. et al. Spin structure of the Shockley surface state on Au(111). *Phys. Rev. B* **69**, 241401 (2004).
6. Yaji, K. et al. Rashba spin splitting of *L*-gap surface states on Ag(111) and Cu(111). *Phys. Rev. B* **98**, 041404 (2018).
7. Mackintosh, A. R. & Andersen, O. K. *Electrons at the Fermi Surface* (ed. Springford, M.) 149 (Cambridge Univ. Press, 1980).
8. Petersen, L. & Hedegård, P. A simple tight-binding model of spin–orbit splitting of *sp*-derived surface states. *Surf. Sci.* **459**, 49–56 (2000).
9. Bihlmayer, G., Koroteev, Y. M., Echenique, P. M., Chulkov, E. V. & Blügel, S. The Rashba-effect at metallic surfaces. *Surf. Sci.* **600**, 3888–3891 (2006).
10. Ishida, H. Rashba spin splitting of Shockley surface states on semi-infinite crystals. *Phys. Rev. B* **90**, 235422 (2014).

11. Winkler, R. Rashba spin splitting in two-dimensional electron and hole systems. *Phys. Rev. B* **62**, 4245–4248 (2000).
12. Ast, C. R. et al. Giant spin splitting through surface alloying. *Phys. Rev. Lett.* **98**, 186807 (2007).
13. Schirone, S. et al. Spin-flip and element-sensitive electron scattering in the $BiAg_2$ surface alloy. *Phys. Rev. Lett.* **114**, 166801 (2015).
14. Ishizaka, K. et al. Giant Rashba-type spin splitting in bulk BiTeI. *Nat. Mater.* **10**, 521–526 (2011).
15. Liebmann, M. et al. Giant Rashba-type spin splitting in ferroelectric GeTe(111). *Adv. Mater.* **28**, 560–565 (2016).
16. Rinaldi, C. et al. Ferroelectric control of the spin texture in GeTe. *Nano Lett.* **18**, 2751–2758 (2018).
17. Sunko, V. et al. Maximal Rashba-like spin splitting via kinetic-energy-coupled inversion-symmetry breaking. *Nature* **549**, 492–496 (2017).
18. Mera Acosta, C., Ogoshi, E., Fazzio, A., Dalpian, G. M. & Zunger, A. The Rashba scale: emergence of band anti-crossing as a design principle for materials with large Rashba coefficient. *Matter* **3**, 145–165 (2020).
19. Dresselhaus, G. Spin–orbit coupling effects in zinc blende structures. *Phys Rev.* **100**, 580–586 (1955).
20. Bernevig, B. A., Orenstein, J. & Zhang, S.-C. Exact SU(2) symmetry and persistent spin helix in a spin–orbit coupled system. *Phys. Rev. Lett.* **97**, 236601 (2006).
21. Zhao, H. J. et al. Purely cubic spin splittings with persistent spin textures. *Phys. Rev. Lett.* **125**, 216405 (2020).
22. Rashba, E. I. & Sheka, V. I. Symmetry of energy bands in crystals of wurtzite type: II. Symmetry of bands including spin-orbit interaction. *Fiz. Tverd. Tela Collected Papers* **2**, 162–176 (1959).
23. Usachov, D. Y. et al. Spin structure of spin–orbit split surface states in a magnetic material revealed by spin-integrated photoemission. *Phys. Rev. B* **101**, 245140 (2020).
24. Usachov, D. Y. et al. Cubic Rashba effect in the surface spin structure of rare-earth ternary materials. *Phys. Rev. Lett.* **124**, 237202 (2020).
25. Friedrich, R., Caciuc, V., Bihlmayer, G., Atodiresei, N. & Blügel, S. Designing the Rashba spin texture by adsorption of inorganic molecules. *New J. Phys.* **19**, 043017 (2017).
26. Wang, F. et al. Switchable Rashba anisotropy in layered hybrid organic–inorganic perovskite by hybrid improper ferroelectricity. *Npj Comput. Mater.* **6**, 183 (2020).
27. Novoselov, K. S., Mishchenko, A., Carvalho, A. & Neto, A. H. C. 2D materials and van der Waals heterostructures. *Science* **353**, aac9439 (2016).
28. Wang, Q. H., Kalantar-Zadeh, K., Kis, A., Coleman, J. N. & Strano, M. S. Electronics and optoelectronics of two-dimensional transition metal dichalcogenides. *Nat. Nanotechnol.* **7**, 699–712 (2012).
29. Gibertini, M., Koperski, M., Morpurgo, A. F. & Novoselov, K. S. Magnetic 2D materials and heterostructures. *Nat. Nanotechnol.* **14**, 408–419 (2019).
30. Du, K. Z. et al. Weak van der Waals stacking, wide-range band gap, and Raman study on ultrathin layers of metal phosphorus trichalcogenides. *ACS Nano* **10**, 1738–1743 (2016).
31. Cheng, Y. C., Zhu, Z. Y., Tahir, M. & Schwingenschlögl, U. Spin–orbit-induced spin splittings in polar transition metal dichalcogenide monolayers. *Europhys. Lett.* **102**, 57001 (2013).
32. Lu, A.-y. et al. Janus monolayers of transition metal dichalcogenides. *Nat. Nanotechnol.* **12**, 744–749 (2017).
33. Zhang, J. et al. Janus monolayer transition-metal dichalcogenides. *ACS Nano* **11**, 8192–8198 (2017).
34. Zhang, L., Yang, Z., Gong, T., Pan, R. & Wang, H. Recent advances in emerging Janus two-dimensional materials: from fundamental physics. *J. Mater. Chem. A* **8**, 8813–8830 (2020).
35. Zhang, X., Liu, Q., Luo, J.-W., Freeman, A. J. & Zunger, A. Hidden spin polarization in inversion-symmetric bulk crystals. *Nat. Phys.* **10**, 387–393 (2014).
36. Riley, J. M. et al. Direct observation of spin-polarized bulk bands in an inversion-symmetric semiconductor. *Nat. Phys.* **10**, 835–839 (2014).
37. Gotlieb, K. et al. Revealing hidden spin–momentum locking in a high-temperature cuprate superconductor. *Science* **362**, 1271–1275 (2018).
38. Zelezny, J. et al. Relativistic Neel-order fields induced by electrical current in antiferromagnets. *Phys. Rev. Lett.* **113**, 157201 (2014).
39. Wadley, P. et al. Electrical switching of an antiferromagnet. *Science* **351**, 587–590 (2016).
40. Bodnar, S. Y. et al. Writing and reading antiferromagnetic Mn_2Au by Neél spin–orbit torques and large anisotropic magnetoresistance. *Nat. Commun.* **9**, 348 (2018).
41. Jungwirth, T. et al. The multiple directions of antiferromagnetic spintronics. *Nat. Phys.* **14**, 200–203 (2018).
42. Baltz, V. et al. Antiferromagnetic spintronics. *Rev. Mod. Phys.* **90**, 015005 (2018).
43. Tanaka, T. et al. Intrinsic spin Hall effect and orbital Hall effect in 4*d* and 5d transition metals. *Phys. Rev. B* **77**, 165117 (2008).
44. Park, S. R., Kim, C. H., Yu, J., Han, J. H. & Kim, C. Orbital-angular-momentum based origin of Rashba-type surface band splitting. *Phys. Rev. Lett.* **107**, 156803 (2011).
45. Go, D. et al. Toward surface orbitronics: giant orbital magnetism from the orbital Rashba effect at the surface of *sp*-metals. *Sci. Rep.* **7**, 46742 (2017).
46. Jo, D., Go, D. & Lee, H.-w Gigantic intrinsic orbital Hall effects in weakly spin–orbit coupled metals. *Phys. Rev. B* **98**, 214405 (2018).
47. Yoda, T., Yokoyama, T. & Murakami, S. Orbital Edelstein effect as a condensed-matter analog of solenoids. *Nano Lett.* **18**, 916–920 (2018).
48. Go, D. et al. Orbital Rashba effect in surface oxidized Cu film. *Phys. Rev. B* **103**, L121113 (2021).
49. Hayami, S., Yanagi, Y. & Kusunose, H. Momentum-dependent spin splitting by collinear antiferromagnetic ordering. *J. Phys. Soc. Jap.* **88**, 123702 (2019).
50. Yuan, L.-d, Wang, Z., Luo, J.-w, Rashba, E. I. & Zunger, A. Giant momentum-dependent spin splitting in centrosymmetric low-*Z* antiferromagnets. *Phys. Rev. B* **102**, 014422 (2020).
51. Yuan, L. D., Wang, Z., Luo, J. W. & Zunger, A. Prediction of low-*Z* collinear and noncollinear antiferromagnetic compounds having momentum-dependent spin splitting even without spin–orbit coupling. *Phys. Rev. Mater.* **5**, 014409 (2021).
52. Šmejkal, L., González-Hernández, R., Jungwirth, T. & Sinova, J. Crystal time-reversal symmetry breaking and spontaneous Hall effect in collinear antiferromagnets. *Sci. Adv.* **6**, eaaz8809 (2020).
53. González-Hernández, R. et al. Efficient electrical spin-splitter based on non-relativistic collinear antiferromagnetism. *Phys. Rev. Lett.* **126**, 127701 (2021).
54. Manchon, A. & Železný, J. Spin polarization without net magnetization. *Physics* **13**, 112 (2020).
55. Železný, J., Zhang, Y., Felser, C. & Yan, B. Spin-polarized current in noncollinear antiferromagnets. *Phys. Rev. Lett.* **119**, 187204 (2017).
56. Hayami, S., Yanagi, Y. & Kusunose, H. Spontaneous antisymmetric spin splitting in noncollinear antiferromagnets without spin–orbit coupling. *Phys. Rev. B* **101**, 220403 (2020).
57. Armitage, N. P., Mele, E. J. & Vishwanath, A. Weyl and Dirac semimetals in three-dimensional solids. *Rev. Mod. Phys.* **90**, 015001 (2018).
58. Hasan, M. et al. Weyl, Dirac and high-fold chiral fermions in topological quantum matter. *Nat. Rev. Mater.* **6**, 784–803 (2021).
59. Oreg, Y., Refael, G. & von Oppen, F. Helical liquids and Majorana bound states in quantum wires. *Phys. Rev. Lett.* **105**, 177002 (2010).
60. Lutchyn, R., Sau, J. & Das Sarma, S. Majorana fermions and a topological phase transition in semiconductor–superconductor heterostructures. *Phys. Rev. Lett.* **105**, 77001 (2010).
61. Mourik, V. et al. Signatures of Majorana fermions in hybrid superconductor–semiconductor nanowire devices. *Science* **336**, 1003–1007 (2012).
62. Vaitiekėnas, S. et al. Flux-induced topological superconductivity in full-shell nanowires. *Science* **367**, eaav3392 (2020).
63. Xu, J.-P. et al. Experimental detection of a Majorana mode in the core of a magnetic vortex inside a topological insulator-superconductor $Bi_2Te_3/NbSe_2$ heterostructure. *Phys. Rev. Lett.* **114**, 017001 (2015).
64. Wang, Z. et al. Evidence for dispersing 1D Majorana channels in an iron-based superconductor. *Science* **367**, 104–108 (2020).
65. Qiao, Z. et al. Quantum anomalous Hall effect in graphene proximity coupled to an antiferromagnetic insulator. *Phys. Rev. Lett.* **112**, 116404 (2014).
66. Lado, J. L. & Fernández-Rossier, J. Quantum anomalous Hall effect in graphene coupled to skyrmions. *Phys. Rev. B* **92**, 115433 (2015).
67. Zanolli, Z. et al. Hybrid quantum anomalous Hall effect at graphene-oxide interfaces. *Phys. Rev. B* **98**, 155404 (2018).
68. Kohno, H. Spintronics with Weyl semimetal. *JPSJ News Comments* **18**, 13 (2021).
69. Fu, L. & Kane, C. L. Topological insulators with inversion symmetry. *Phys. Rev. B* **76**, 045302 (2007).
70. Moore, J. E. & Balents, L. Topological invariants of time-reversal-invariant band structures. *Phys. Rev. B* **75**, 121306(R) (2007).
71. Bansil, A., Lin, H. & Das., T. Colloquium: topological band theory. *Rev. Mod. Phys.* **88**, 021004 (2016).
72. Eremeev, S. V., Koroteev, Y. M. & Chulkov, E. V. Effect of the atomic composition of the surface on the electron surface states in topological insulators A_2B_3. *JETP Lett.* **91**, 387–391 (2010).
73. Fu, L. Hexagonal warping effects in the surface states of the topological insulator Bi_2Te_3. *Phys. Rev. Lett.* **103**, 266801 (2009).
74. Basak, S. et al. Spin texture on the warped Dirac-cone surface states in topological insulators. *Phys. Rev. B.* **84**, 121401(R) (2011).
75. Henk, J. et al. Complex spin texture in the pure and Mn-doped topological insulator Bi_2Te_3. *Phys. Rev. Lett.* **108**, 206801 (2012).
76. Johansson, A., Henk, J. & Mertig, I. Edelstein effect in Weyl semimetals. *Phys. Rev. B* **97**, 085417 (2018).
77. Qi, X.-L., Hughes, T. L. & Zhang, S.-C. Topological field theory of time-reversal invariant insulators. *Phys. Rev. B* **78**, 195424 (2008).
78. Deng, H. et al. High-temperature quantum anomalous Hall regime in a $MnBi_2Te_4/Bi_2Te_3$ superlattice. *Nat. Phys.* **17**, 36–42 (2021).
79. Henk, J. et al. Topological character and magnetism of the Dirac state in Mn doped Bi_2Te_3. *Phys. Rev. Lett.* **109**, 076801 (2012).
80. Petrov, E. K. et al. Domain wall induced spin-polarized flat bands in antiferromagnetic topological insulators. *Phys. Rev. B* **103**, 235142 (2021).
81. Rusinov, I. P., Men'shov, V. N. & Chulkov, E. V. Spectral features of magnetic domain walls on the surface of three-dimensional topological insulators. *Phys. Rev. B* **104**, 035411 (2021).
82. Liu, Q., Liu, C.-X., Xu, C., Qi, X. & Zhang, S. C. Magnetic impurities on the surface of a topological insulator. *Phys. Rev. Lett.* **102**, 156603 (2009).
83. Polyakov, A. et al. Surface alloying and iron selenide formation in $Fe/Bi_2Se_3(0001)$ observed by X-ray absorption fine structure experiments. *Phys. Rev. B* **92**, 045423 (2015).
84. Chen, Y. L. et al. Massive Dirac fermion on the surface of a magnetically doped topological insulator. *Science* **329**, 659–662 (2010).
85. Lee, I. et al. Imaging Dirac-mass disorder from magnetic dopant atoms in the ferromagnetic topological insulator $Cr_x(Bi_{0.1}Sb_{0.9})_{2-x}Te_3$. *Proc. Natl Acad. Sci. USA* **112**, 1316–1321 (2015).
86. Chang, C.-Z. et al. Experimental observation of the quantum anomalous Hall effect in a magnetic topological insulator. *Science* **340**, 167–170 (2013).
87. Mogi, M. et al. Magnetic modulation doping in topological insulators toward higher-temperature quantum anomalous Hall effect. *Appl. Phys. Lett.* **107**, 182401 (2015).
88. Chang, C.-Z. et al. High-precision realization of robust quantum anomalous Hall state in a hard ferromagnetic topological insulator. *Nat. Mater.* **14**, 473–477 (2015).
89. Mogi, M. et al. A magnetic heterostructure of topological insulators as a candidate for an axion insulator. *Nat. Mater.* **16**, 516–521 (2017).
90. Otrokov, M. M. et al. Highly-ordered wide bandgap materials for quantized anomalous Hall and magnetoelectric effects. *2D Mater.* **4**, 025082 (2017).
91. Hirahara, T. et al. Large-gap magnetic topological heterostructure formed by subsurface incorporation of a ferromagnetic layer. *Nano Lett.* **17**, 3493–3500 (2017).
92. Otrokov, M. M. et al. Magnetic extension as an efficient method for realizing the quantum anomalous Hall state in topological insulators. *JETP Lett.* **105**, 297–302 (2017).
93. Hagmann, J. A. et al. Molecular beam epitaxy growth and structure of self-assembled Bi_2Se_3/Bi_2MnSe_4 multilayer heterostructures. *New J. Phys.* **19**, 085002 (2017).
94. Hirahara, T. et al. Fabrication of a novel magnetic topological heterostructure and temperature evolution of its massive Dirac cone. *Nat. Commun.* **11**, 4821 (2020).
95. Otrokov, M. M. et al. Prediction and observation of an antiferromagnetic topological insulator. *Nature* **576**, 416–422 (2019).
96. Klimovskikh, I. I. et al. Tunable 3D/2D magnetism in the $(MnBi_2Te_4)(Bi_2Te_3)_m$ topological insulators family. *npj Quantum Mater.* **5**, 54 (2020).

97. Eremeev, S. V. et al. Topological magnetic materials of the $(MnSb_2Te_4)\cdot(Sb_2Te_3)_n$ van der Waals compounds family. *J. Phys. Chem. Lett.* **12**, 4268 (2021).
98. Wimmer, S. et al. Mn-rich $MnSb_2Te_4$: a topological insulator with magnetic gap closing at high Curie temperatures of 45–50 K. *Adv. Mater*. https://doi.org/10.1002/adma.202102935 (2021).
99. Wang, Z. et al. Time-reversal-breaking Weyl fermions in magnetic Heusler alloys. *Phys. Rev. Lett.* **117**, 236401 (2016).
100. Wang, Q. et al. Large intrinsic anomalous Hall effect in half-metallic ferromagnet $Co_3Sn_2S_2$ with magnetic Weyl fermions. *Nat. Commun.* **9**, 3681 (2018).
101. Nakatsuji, S., Kiyohara, N. & Higo, T. Large anomalous Hall effect in a non-collinear antiferromagnet at room temperature. *Nature* **527**, 212–215 (2015).
102. Chen, T. et al. Anomalous transport due to Weyl fermions in the chiral antiferromagnets Mn_3X, X = Sn, Ge. *Nat. Commun.* **12**, 572 (2021).
103. Li, Y. et al. Correlated magnetic Weyl semimetal state in strained $Pr_2Ir_2O_7$. *Adv. Mater.* **33**, 2008528 (2021).
104. Stewart, G. R. Heavy-fermion systems. *Rev. Mod. Phys.* **56**, 755–787 (1984).
105. Stewart, G. R. Non-Fermi-liquid behavior in *d*- and *f*-electron metals. *Rev. Mod. Phys.* **73**, 797–855 (2001).
106. Khanh, N. D. et al. Nanometric square skyrmion lattice in a centrosymmetric tetragonal magnet. *Nat. Nanotechnol.* **15**, 444–449 (2020).
107. Ernst Bauer, E. & Sigrist, M. *Non-Centrosymmetric Superconductors: Introduction and Overview* https://doi.org/10.1007/978-3-642-24624-1 (Springer, 2012).
108. Generalov, A. et al. Strong spin–orbit coupling in the noncentrosymmetric Kondo lattice. *Phys. Rev. B* **98**, 115157 (2018).
109. Generalov, A. et al. Spin orientation of two-dimensional electrons driven by temperature-tunable competition of spin–orbit and exchange magnetic interactions. *Nano Lett.* **17**, 811–820 (2017).
110. Schulz, S. et al. Emerging 2D-ferromagnetism and strong spin–orbit coupling at the surface of valence-fluctuating $EuIr_2Si_2$. *npj Quant. Mat.* **4**, 26 (2019).
111. Schulz, S. et al. Classical and cubic Rashba effect in the presence of in-plane 4*f* magnetism at the iridium silicide surface of the antiferromagnet $GdIr_2Si_2$. *Phys. Rev. B* **103**, 035123 (2021).
112. Michishita, Y. & Peters, R. Impact of the Rashba spin–orbit coupling on *f*-electron materials. *Phys. Rev. B* **99**, 155141 (2019).
113. Peters, R. & Yanas, Y. Strong enhancement of the Edelstein effect in *f* -electron system. *Phys. Rev. B* **97**, 115128 (2018).
114. Usachov, D. Y. et al. Photoelectron diffraction for probing valency and magnetism of 4*f*-based materials: a view on valence-fluctuating $EuIr_2Si_2$. *Phys. Rev. B* **102**, 205102 (2020).
115. Güttler, M. et al. Robust and tunable itinerant ferromagnetism at the silicon surface of the antiferromagnet $GdRh_2Si_2$. *Sci. Rep.* **6**, 24254 (2016).
116. Mende, M. et al. Strong Rashba effect and different *f*–*d* hybridization phenomena at the surface of the heavy-fermion superconductor $CeIrIn_5$. *Adv. Electron. Mater*. https://doi.org/10.1002/aelm.202100768 (2021).
117. Goh, S. K. et al. Anomalous upper critical field in $CeCoIn_5$/$YbCoIn_5$ superlattices with a Rashba-type heavy fermion interface. *Phys. Rev. Lett.* **109**, 157006 (2012).
118. Shimozawa, M. et al. Controllable Rashba spin–orbit interaction in artificially engineered superlattices involving the heavy-fermion superconductor $CeCoIn_5$. *Phys. Rev. Lett.* **112**, 156404 (2014).
119. Yang, H., Yang, S.-H., Takahashi, S., Maekawa, S. & Parkin, S. S. P. Extremely long quasiparticle spin lifetimes in superconducting aluminium using MgO tunnel spin injectors. *Nat. Mater.* **9**, 586–593 (2010).
120. Linder, J. & Robinson, W. A. J. Superconducting spintronics. *Nat. Phys.* **11**, 307–315 (2015).
121. He, W.-Y. & Law, K. T. Magnetoelectric effects in gyrotropic superconductors. *Phys. Rev. Res.* **2**, 012073 (2020).
122. Ikeda, Y. & Yanase, Y. Giant surface edelstein effect in *d*-wave superconductors. *Phys. Rev. B* **102**, 214510 (2020).
123. Guang, Y., Ciccarelli, C. & Robinson, W. A. J. Boosting spintronics with superconductivity. *APL Mater.* **9**, 050703 (2021).
124. Gor'kov, L. P. & Rashba, E. I. Superconducting 2D system with lifted spin degeneracy: mixed singlet–triplet state. *Phys. Rev. Lett.* **87**, 37004 (2001).
125. Shang, T. & Shiroka, T. Time-reversal symmetry breaking in Re-based superconductors: recent developments. *Front. Phys.* **9**, 651163 (2021).
126. Yip, S. Noncentrosymmetric superconductors. *Annu. Rev. Condens. Matter Phys.* **5**, 15–33 (2014).
127. Khim, S. et al. Field-induced transition within the superconducting state of $CeRh_2As_2$. *Science* **373**, 1012–1016 (2021).
128. Nichele, F. et al. Scaling of Majorana zero-bias conductance peaks. *Phys. Rev. Lett.* **119**, 136803 (2017).
129. Zhang, H., Liu, D. E., Wimmer, M. & Kouwenhoven, L. P. Next steps of quantum transport in Majorana nanowire devices. *Nat. Commun.* **10**, 5128 (2019).
130. Manchon, A. & Zhang, S. Theory of nonequilibrium intrinsic spin torque in a single nanomagnet. *Phys. Rev. B* **78**, 212405 (2008).
131. Mihai Miron, I. et al. Current-driven spin torque induced by the Rashba effect in a ferromagnetic metal layer. *Nat. Mater.* **9**, 230–234 (2010).
132. Manchon, A. et al. Current-induced spin–orbit torques in ferromagnetic and antiferromagnetic systems. *Rev. Mod. Phys.* **91**, 035004 (2019).
133. Pham, V. T. et al. Spin–orbit magnetic state readout in scaled ferromagnetic/heavy metal nanostructures. *Nat. Electron.* **3**, 309–315 (2020).
134. Seifert, T. et al. Efficient metallic spintronic emitters of ultrabroadband terahertz radiation. *Nat. Photonics* **10**, 483–488 (2016).
135. Ivchenko, E. L. & Pikus, G. E. New photogalvanic effect in gyrotropic crystals. *Pis'ma Zh. Eksp. Teor. Fiz.* **27**, 604 (1978).
136. Vorob'ev, L. E. et al. Optical activity in tellurium induced by a current. *JETP Lett.* **29**, 441 (1979).
137. Edelstein, V. M. Spin polarization of conduction electrons induced by electric current in two-dimensional asymmetric electron systems. *Solid State Commun.* **73**, 233–235 (1990).
138. Kato, Y. K., Myers, R., Gossard, A. & Awschalom, D. D. Current-induced spin polarization in strained semiconductors. *Phys. Rev. Lett.* **93**, 176601 (2004).
139. Ivchenko, E. L., Lyanda-Geller, Y. B. & Pikus, G. E. Circular magnetophotocurrent and spin splitting of band states in optically-inactive crystals. *Solid State Commun.* **69**, 663–665 (1989).
140. Ganichev, S. D. et al. Spin-galvanic effect. *Nature* **417**, 153–156 (2002).
141. Ghosh, S. & Manchon, A. Spin–orbit torque in a three-dimensional topological insulator–ferromagnet heterostructure: crossover between bulk and surface transport. *Phys. Rev. B* **97**, 134402 (2018).
142. Li, P. et al. Spin–momentum locking and spin–orbit torques in magnetic nano-heterojunctions composed of Weyl semimetal WTe_2. *Nat. Commun.* **9**, 3990 (2018).
143. Sinova, J., Valenzuela, S. O., Wunderlich, J., Back, C. H. & Jungwirth, T. Spin Hall effect. *Rev. Mod. Phys.* **87**, 1213 (2015).
144. Du, Y. et al. Disentanglement of spin–orbit torques in Co/Pt bilayers with the presence of spin Hall effect and Rashba–Edelstein effect. *Phys. Rev. Appl.* **13**, 054014 (2020).
145. Rojas-Sánchez, J.-C. & Fert, A. Compared efficiencies of conversions between charge and spin current by spin–orbit interactions in two- and three-dimensional systems. *Phys. Rev. Appl.* **11**, 054049 (2019).
146. Sánchez, J. C. R. et al. Spin-to-charge conversion using Rashba coupling at the interface between non-agnetic materials. *Nat. Commun.* **4**, 2944 (2013).
147. Zhang, H. J. et al. Charge-to-spin conversion and spin diffusion in Bi/Ag bilayers observed by spin-polarized positron beam. *Phys. Rev. Lett.* **114**, 166602 (2015).
148. Jungfleisch, M. B. et al. Interface-driven spin-torque ferromagnetic resonance by Rashba coupling at the interface between nonmagnetic materials. *Phys. Rev. B* **93**, 224419 (2016).
149. Nakayama, H. et al. Rashba–Edelstein magnetoresistance in metallic heterostructures. *Phys. Rev. Lett.* **117**, 116602 (2016).
150. Jungfleisch, M. B. et al. Control of terahertz emission by ultrafast spin-charge current conversion at Rashba interfaces. *Phys. Rev. Lett.* **120**, 207207 (2018).
151. Zhang, W., Jungfleisch, M. B., Jiang, W., Pearson, J. E. & Hoffmann, A. Spin pumping and inverse Rashba–Edelstein effect in NiFe/Ag/Bi and NiFe/Ag/Sb. *J. Appl. Phys.* **117**, 17C727 (2015).
152. Karube, S., Kondou, K. & Otani, Y. Experimental observation of spin-to-charge current conversion at non-magnetic metal/Bi_2O_3 interfaces. *Appl. Phys. Express* **9**, 033001 (2016).
153. Sangiao, S. et al. Control of the spin to charge conversion using the inverse Rashba–Edelstein effect. *Appl. Phys. Lett.* **106**, 172403 (2015).
154. Zhou, C. et al. Broadband terahertz generation via the interface inverse Rashba–Edelstein effect. *Phys. Rev. Lett.* **121**, 086801 (2018).
155. Matsushima, M. et al. Quantitative investigation of the inverse Rashba–Edelstein effect in Bi/Ag and Ag/Bi on YIG. *Appl. Phys. Lett.* **110**, 072404 (2017).
156. Shen, J. et al. Spin-to-charge conversion in Ag/Bi bilayer revisited. *Phys. Rev. Lett.* **126**, 197201 (2021).
157. Mellnik, A. R. et al. Spin-transfer torque generated by a topological insulator. *Nature* **511**, 449–451 (2014).
158. Fan, Y. et al. Magnetization switching through giant spin–orbit torque in a magnetically doped topological insulator heterostructure. *Nat. Mater.* **13**, 699–704 (2014).
159. Wang, Y. et al. Topological surface states originated spin–orbit torques in Bi_2Se_3. *Phys. Rev. Lett.* **114**, 257202 (2015).
160. Han, J. et al. Room-temperature spin–orbit torque switching induced by a topological insulator. *Phys. Rev. Lett.* **119**, 077702 (2017).
161. Dc, M. et al. Room-temperature high spin–orbit torque due to quantum confinement in sputtered $Bi_xSe_{(1-x)}$ films. *Nat. Mater.* **17**, 800–807 (2018).
162. Bonell, F. et al. Control of spin–orbit torques by interface engineering in topological insulator heterostructures. *Nano Lett.* **20**, 5893–5899 (2020).
163. Han, J. & Liu, L. Topological insulators for efficient spin–orbit torques. *APL Mater.* **9**, 060901 (2021).
164. Shiomi, Y. et al. Spin-electricity conversion induced by spin injection into topological insulators. *Phys. Rev. Lett.* **113**, 196601 (2014).
165. Wang, H. et al. Surface-state-dominated spin-charge current conversion in topological-insulator–ferromagnetic-insulator heterostructures. *Phys. Rev. Lett.* **117**, 076601 (2016).
166. Mendes, J. B. S. et al. Unveiling the spin-to-charge current conversion signal in the topological insulator Bi_2Se_3 by means of spin pumping experiments. *Phys. Rev. Mater.* **5**, 024206 (2021).
167. Rojas-Sánchez, J.-C. et al. Spin to charge conversion at room temperature by spin pumping into a new type of topological insulator: α-Sn films. *Phys. Rev. Lett.* **116**, 096602 (2016).
168. Zhang, S. & Fert, A. Conversion between spin and charge currents with topological insulators. *Phys. Rev. B* **94**, 184423 (2016).
169. Isshiki, H., Muduli, P., Kim, J., Kondou, K. & Otani, Y. Phenomenological model for the direct and inverse Edelstein effects. *Phys. Rev. B* **102**, 184411 (2020).
170. Lesne, E. et al. Highly efficient and tunable spin-to-charge conversion through Rashba coupling at oxide interfaces. *Nat. Mater.* **15**, 1261–1266 (2016).
171. Vaz, D. C. et al. Mapping spin-charge conversion to the band structure in a topological oxide two-dimensional electron gas. *Nat. Mater.* **18**, 1187–1193 (2019).
172. Ohya, S. et al. Efficient intrinsic spin-to-charge current conversion in an all-epitaxial single-crystal perovskite-oxide heterostructure of $La_{0.67}Sr_{0.33}MnO_3$/$LaAlO_3$/$SrTiO_3$. *Phys. Rev. Res.* **2**, 012014 (2020).
173. Vaz, D. C. et al. Determining the Rashba parameter from the bilinear magnetoresistance response in a two-dimensional electron gas. *Phys. Rev. Mater.* **4**, 071001 (2020).
174. Noël, P. et al. Non-volatile electric control of spin-charge conversion in a $SrTiO_3$ Rashba system. *Nature* **580**, 483–486 (2020).
175. Varotto, S. et al. Room-temperature ferroelectric switching of spin-to-charge conversion in germanium telluride. *Nat. Electronics* **4**, 740–747 (2021).
176. Zhu, L., Ralph, D. C. & Buhrman, R. A. Highly efficient spin-current generation by the spin Hall effect in $Au_{1-x}Pt_x$. *Phys. Rev. Appl.* **10**, 031001 (2018).
177. Khang, N. H. D., Ueda, Y. & Hai, P. N. A conductive topological insulator with large spin Hall effect for ultralow power spin–orbit torque switching. *Nat. Mater.* **17**, 808–813 (2018).
178. Manipatruni, S. et al. Scalable energy-efficient magnetoelectric spin–orbit logic. *Nature* **565**, 35–42 (2019).
179. Wang, X. et al. Ultrafast spin-to-charge conversion at the surface of topological insulator thin films. *Adv. Mater.* **30**, 1802356 (2018).
180. Rikken, G. L. & Wyder, P. Magnetoelectric anisotropy in diffusive transport. *Phys. Rev. Lett.* **94**, 016601 (2005).
181. Pop, F., Auban-Senzier, P., Canadell, E., Rikken, G. L. & Avarvari, N. Electrical magnetochiral anisotropy in a bulk chiral molecular conductor. *Nat. Commun.* **5**, 3757 (2014).
182. Ideue, T. et al. Bulk rectification effect in a polar semiconductor. *Nat. Phys.* **13**, 578–583 (2017).

183. Guillet, T. et al. Observation of large unidirectional Rashba magnetoresistance in Ge(111). *Phys. Rev. Lett.* **124**, 027201 (2020).
184. Choe, D. et al. Gate-tunable giant nonreciprocal charge transport in noncentrosymmetric oxide interfaces. *Nat. Commun.* **10**, 4510 (2019).
185. He, P. et al. Bilinear magnetoelectric resistance as a probe of three-dimensional spin texture in topological surface states. *Nat. Phys.* **14**, 495–499 (2018).
186. He, P. et al. Nonlinear magnetotransport shaped by Fermi surface topology and convexity. *Nat. Commun.* **10**, 1290 (2019).
187. Yasuda, K. et al. Nonreciprocal charge transport at topological insulator/superconductor interface. *Nat. Commun.* **10**, 2734 (2019).
188. Ideue, T., Koshikawa, S., Namiki, H., Sasagawa, T. & Iwasa, Y. Giant nonreciprocal magnetotransport in bulk trigonal superconductor $PbTaSe_2$. *Phys. Rev. Res.* **2**, 042046(R) (2020).
189. Itahashi, Y. M. et al. Nonreciprocal transport in gate-induced polar superconductor $SrTiO_3$. *Sci. Adv.* **6**, eaay9120 (2020).
190. He, P. et al. Nonlinear planar Hall effect. *Phys. Rev. Lett.* **123**, 016801 (2019).
191. Olejník, K., Novák, V., Wunderlich, J. & Jungwirth, T. Electrical detection of magnetization reversal without auxiliary magnets. *Phys. Rev. B* **91**, 180402(R) (2015).
192. Železný, J. et al. Unidirectional magnetoresistance and spin–orbit torque in NiMnSb. *Phys. Rev. B* **104**, 054429 (2021).
193. Avci, C. O. et al. Unidirectional spin Hall magnetoresistance in ferromagnet/normal metal bilayers. *Nat. Phys.* **11**, 570–575 (2015).
194. Yasuda, K. et al. Large unidirectional magnetoresistance in a magnetic topological insulator. *Phys. Rev. Lett.* **117**, 127202 (2016).
195. Lv, Y. et al. Unidirectional spin-Hall and Rashba–Edelstein magnetoresistance in topological insulator-ferromagnet layer heterostructures. *Nat. Commun.* **9**, 111 (2018).
196. Avci, C. O., Mendil, J., Beach, G. S. D. & Gambardella, P. Origins of the unidirectional spin Hall magnetoresistance in metallic bilayers. *Phys. Rev. Lett.* **121**, 087207 (2018).
197. Kang, K., Li, T., Sohn, E., Shan, J. & Mak, K. F. Nonlinear anomalous Hall effect in few-layer WTe_2. *Nat. Mater.* **18**, 324–328 (2019).
198. Ma, Q. et al. Observation of the nonlinear Hall effect under time-reversal-symmetric conditions. *Nature* **565**, 337–342 (2019).
199. Kumar, D. et al. Room-temperature nonlinear Hall effect and wireless radiofrequency rectification in Weyl semimetal $TaIrTe_4$. *Nat. Nanotechnol.* **16**, 421–425 (2021).
200. Dzsaber, S. et al. Giant spontaneous Hall effect in a nonmagnetic Weyl–Kondo semimetal. *Proc. Natl Acad. Sci. USA* **118**, e2013386118 (2021).
201. Sodemann, I. & Fu, L. Quantum nonlinear Hall effect induced by Berry curvature dipole in time-reversal invariant materials. *Phys. Rev. Lett.* **115**, 216806 (2015).
202. Du, Z. Z., Wang, C. M., Sun, H. P., Lu, H. Z. & Xie, X. C. Quantum theory of the nonlinear Hall effect. *Nat. Commun.* **12**, 5038 (2021).
203. Zhang, Y. & Fu, L. Terahertz detection based on nonlinear Hall effect without magnetic field. *Proc. Natl Acad. Sci. USA* **118**, e2100736118 (2021).
204. Tokura, Y. & Nagaosa, N. Nonreciprocal responses from non-centrosymmetric quantum materials. *Nat. Commun.* **9**, 3740 (2018).
205. Morimoto, T. & Nagaosa, N. Topological nature of nonlinear optical effects in solids. *Sci. Adv.* **2**, e1501524 (2016).
206. Côté, D., Laman, N. & van Driel, H. M. Rectification and shift currents in GaAs. *Appl. Phys. Lett.* **80**, 905 (2002).
207. Grinberg, I. et al. Perovskite oxides for visible-light-absorbing ferroelectric and photovoltaic materials. *Nature* **503**, 509–512 (2013).
208. Nakamura, M. et al. Shift current photovoltaic effect in a ferroelectric charge-transfer complex. *Nat. Commun.* **8**, 281 (2017).
209. McIver, J. W., Hsieh, D., Steinberg, H., Jarillo-Herrero, P. & Gedik, N. Control over topological insulator photocurrents with light polarization. *Nat. Nanotechnol.* **7**, 96–100 (2012).
210. Jozwiak, C. et al. Photoelectron spin-flipping and texture manipulation in a topological insulator. *Nat. Phys.* **9**, 293–298 (2013).
211. Braun, L. et al. Ultrafast photocurrents at the surface of the three-dimensional topological insulator Bi_2Se_3. *Nat. Commun.* **7**, 13259 (2016).
212. Zheng, F., Tan, L. Z., Liu, S. & Rappe, A. M. Rashba spin–orbit coupling enhanced carrier lifetime in $CH_3NH_3PbI_3$. *Nano Lett.* **15**, 7794 (2015).
213. Wang, J. et al. Spin-optoelectronic devices based on hybrid organic–inorganic trihalide perovskites. *Nat. Commun.* **10**, 129 (2019).
214. Niesner, D. et al. Giant Rashba splitting in $CH_3NH_3PbBr_3$ organic–inorganic perovskite. *Phys. Rev. Lett.* **117**, 126401 (2016).
215. Kepenekian, M. et al. Rashba and Dresselhaus effects in hybrid organic–inorganic perovskites: from basics to devices. *ACS Nano* **9**, 11557–11567 (2015).
216. Etienne, T., Mosconi, E. & Angelis, F. D. Dynamical origin of the Rashba effect in organohalide lead perovskites: a key to suppressed carrier recombination in perovskite solar cells? *J. Phys. Chem. Lett.* **7**, 1638–1645 (2016).
217. Nitta, J., Akazaki, T., Takayanagi, H. & Enoki, T. Gate control of spin–orbit interaction in an inverted InGaAs/InAlAs hetrostructure. *Phys. Rev. Lett.* **78**, 1335 (1997).
218. Cheng, L. et al. Optical manipulation of Rashba spin–orbit coupling at $SrTiO_3$-based oxide interfaces. *Nano Lett.* **17**, 6534 (2017).
219. Michiardi, M. et al. Optical manipulation of Rashba-split 2-dimensional electron gas. *Nat Commun.* **13**, 3096 (2022).
220. Lindner, N. H., Refael, G. & Galitski, V. Floquet topological insulator in semiconductor quantum wells. *Nat. Phys.* **7**, 490–495 (2011).
221. Wang, Y. H., Steinberg, H., Jarillo-Herrero, P. & Gedik, N. Observation of Floquet–Bloch states on the surface of a topological insulator. *Science* **342**, 453–457 (2013).
222. Mciver, J. W. et al. Light-induced anomalous Hall effect in graphene. *Nat. Phys.* **16**, 38–41 (2020).
223. Hernangómez-Pérez, D., Torres, J. D. & López, A. Photoinduced electronic and spin properties of two-dimensional electron gases with Rashba spin–orbit coupling under perpendicular magnetic fields. *Phys. Rev. B* **102**, 165414 (2020).
224. King, P. D. C. et al. Large tunable Rashba spin splitting of a two-dimensional electron gas in Bi_2Se_3. *Phys. Rev. Lett.* **107**, 096802 (2011).
225. Curtarolo, S. et al. The high-throughput highway to computational materials design. *Nat. Mater.* **12**, 191–201 (2013).
226. Mounet, N. et al. Two-dimensional materials from high-throughput computational exfoliation of experimentally known compounds. *Nat. Nanotechnol.* **13**, 246–252 (2018).
227. Vergniory, M. G. et al. A complete catalogue of high-quality topological materials. *Nature* **566**, 480–485 (2019).
228. Zhang, T. et al. Catalogue of topological electronic materials. *Nature* **566**, 475–479 (2019).
229. Xu, Y. et al. High-throughput calculations of magnetic topological materials. *Nature* **586**, 702–707 (2020).
230. Schliemann, J., Egues, J. C. & Loss, D. Nonballistic spin-field-effect transistor. *Phys. Rev. Lett.* **90**, 146801 (2003).
231. Lysne, M., Murakami, Y., Sch, M. & Werner, P. High-harmonic generation in spin–orbit coupled systems. *Phys. Rev. B* **102**, 081121 (2020).
232. Ly, O. & Manchon, A. Spin–orbit coupling induced ultra-high harmonic generation from magnetic dynamics. *Phys. Rev. B* **105**, L180415 (2022).
233. Shao, D.-f, Zhang, S.-h, Gurung, G., Yang, W. & Tsymbal, E. Y. Nonlinear anomalous Hall effect for Neel vector detection. *Phys. Rev. Lett.* **124**, 67203 (2020).
234. Galitski, V. & Spielman, I. B. Spin–orbit coupling in quantum gases. *Nature* **494**, 49–54 (2013).
235. El-Ganainy, R. et al. Non-Hermitian physics and PT symmetry. *Nat. Phys.* **14**, 11–19 (2018).
236. Lee, C. H. et al. Topolectrical circuits. *Commun. Phys.* **1**, 39 (2018).
237. Carbone, C. et al. Asymmetric band gaps in a Rashba film system. *Phys. Rev. B* **93**, 125409 (2016).
238. Imamura, H., Bruno, P. & Utsumi, Y. Twisted exchange interaction between localized spins embedded in a one- or two-dimensional electron gas with Rashba spin–orbit coupling. *Phys. Rev. B* **69**, 121303 (2004).
239. Kundu, A. & Zhang, S. Dzyaloshinskii–Moriya interaction mediated by spin-polarized band with Rashba spin–orbit coupling. *Phys. Rev. B* **92**, 094434 (2015).
240. Barnes, S., Ieda, J. & Maekawa, S. Rashba spin–orbit anisotropy and the electric field control of magnetism. *Sci. Rep.* **4**, 4105 (2014).

Acknowledgements
The authors thank F. Nasr for her critical reading of the manuscript. P.N. acknowledges the support of the ETH Zurich Postdoctoral Fellowship Program 19-2 FEL-61. A.M. acknowledges support from the Excellence Initiative of Aix-Marseille Université–A*Midex, a French 'Investissements d'Avenir' program.

Author contributions
The authors contributed equally to all aspects of the article.

Competing interests
The authors declare no competing interests.

Peer review information
Nature Reviews Physics thanks the anonymous referees for their contribution to the peer review of this work.

Publisher's note
Springer Nature remains neutral with regard to jurisdictional claims in published maps and institutional affiliations.

Supplementary information
The online version contains supplementary material available at https://doi.org/10.1038/s42254-022-00490-y.